Effect of viscosity on the shaking-induced fluidization in a liquid-immersed granular medium

Nao Yasuda and Ikuro Sumita*

Earth and Environmental Sciences Course, Division of Natural System, Graduate School of Natural Science and Technology, Kanazawa University, Kanazawa 920-1192, Japan

(Received 15 May 2015; revised manuscript received 26 December 2015; published 3 February 2016)

A liquid-immersed granular medium is shaken vertically under a wide range of accelerations (Γ in dimensionless form) and frequencies (f) and its fluidization process is studied. The granular medium is formed by settling and consists of two size-graded layers (particle diameter d) such that the upper layer is fine grained and is less permeable. When $\Gamma > \Gamma_c$, a liquid-rich layer formed by the accumulated liquid at the two-layer boundary causes a gravitational instability. The upwellings of the instability are separated horizontally by a distance (wavelength) λ, and their amplitude grows exponentially with time [$\propto \exp(pt)$] at a growth rate p. We conduct experiments for two liquid viscosity cases such that the particle settling velocity (V_s) of the same particle differs by a factor of 17. We find that for both cases, Γ_c is at a minimum in an optimum frequency band centered at $f \sim 100$ Hz. However, the high-viscosity (HV) case has a smaller Γ_c, a shorter λ, and a faster dimensionless growth rate [$p' = p/(V_s/d)$]. We also measure granular rheology under an oscillatory shear and find that (i) interparticle friction decreases when the strain amplitude becomes large and (ii) friction is smaller for the HV case. From (i), we infer that the shear strain of the shaking experiments becomes largest at around $f \sim 100$ Hz. We consider that (ii) is a consequence of liquid lubrication and is a reason for a smaller Γ_c for the HV case. We show that the low- and high-frequency limits of the optimum frequency band can be explained by introducing critical values of dimensionless jerk (i.e., time derivative of acceleration) J and dimensionless shaking energy S. The low-frequency limit corresponds to the requirement that in order to unjam the particles, the period of shaking ($1/f$) must be shorter than the time needed for the particles to rearrange by settling (d/V_s), which also explains why the HV case is fluidized at a lower f compared to the LV case. We apply the results of the linear stability analyses for Rayleigh-Taylor instability. Using the measured λ and p, we infer that (i) only a thin layer beneath the two-layer boundary is mobile and the rest of the lower layer remains jammed and (ii) the effective viscosity of the upper granular layer relative to the liquid is smaller for the HV case as a result of smaller friction.

DOI: 10.1103/PhysRevE.93.022901

I. INTRODUCTION

When a liquid-immersed granular medium is shaken strongly enough, the interparticle contact is loosened and the medium becomes fluidized (e.g., [1]). This situation is commonly realized when earthquakes occur and is called liquefaction. Consequences of liquefaction appear as eruption of ground water which form mud volcanoes and water-escape structures. Laboratory experiments show that such structures form by a channelized upward flow in a layered sediment in which the upper layer is less permeable (e.g., [2]). Recently we similarly showed [3] that spectacular instabilities occur when a water-immersed granular medium with a less permeable upper layer is shaken vertically. Such a layered medium is suited to quantifying the degree of fluidization because the resulting instabilities are clearly visualized. From measuring the amplitude of the instability, we showed that there is an optimum frequency band of shaking centered at $\sim$100 Hz in which the instability grows under a smallest acceleration.

Shaking-induced fluidization may even occur in a granular medium in which the liquid is more viscous than water, such as in crystal-bearing magma and oil sands and when the liquid suspends fine particles such that the effective viscosity of the liquid becomes larger. In the case of magma, observations show that fluidization can even trigger volcanic eruptions [4]. Although there have been several shaking experiments using water-immersed granular medium (e.g., [5–7]), little is understood about how the nature of fluidization and the required shaking condition differ when the liquid viscosity is changed.

Here we extend our previous study using a high-viscosity liquid and clarify how the results change. We conduct comprehensive image analyses by using not only the amplitude of the instability but also its growth rate and the horizontal spacing (wavelength) of the upwellings, as well as the vertical compaction of the granular medium. These results are compared with the estimates obtained from the linear stability analysis of Rayleigh-Taylor instability and from the compaction estimated using Darcy's law for permeable flow. Furthermore, to complement the shaking experiments and to better understand their results, we conduct rheology measurements of a liquid-immersed granular medium under an oscillatory shear. Combining these results, we attempt to explain the origin of the viscosity dependence.

II. EXPERIMENTAL METHOD

A. Shaking experiments

Figure 1(a) shows the experimental setup. A rectangular cell with a width of 99.4 mm, a height of $H = 107.6$ mm, and a thickness of 22.0 mm is filled with a mixture of spherical glass beads and liquid. Glass beads with two diameters (d) are used: coarse ($d = 0.22 \pm 0.04$ mm) red particles and fine

*isumita@staff.kanazawa-u.ac.jp

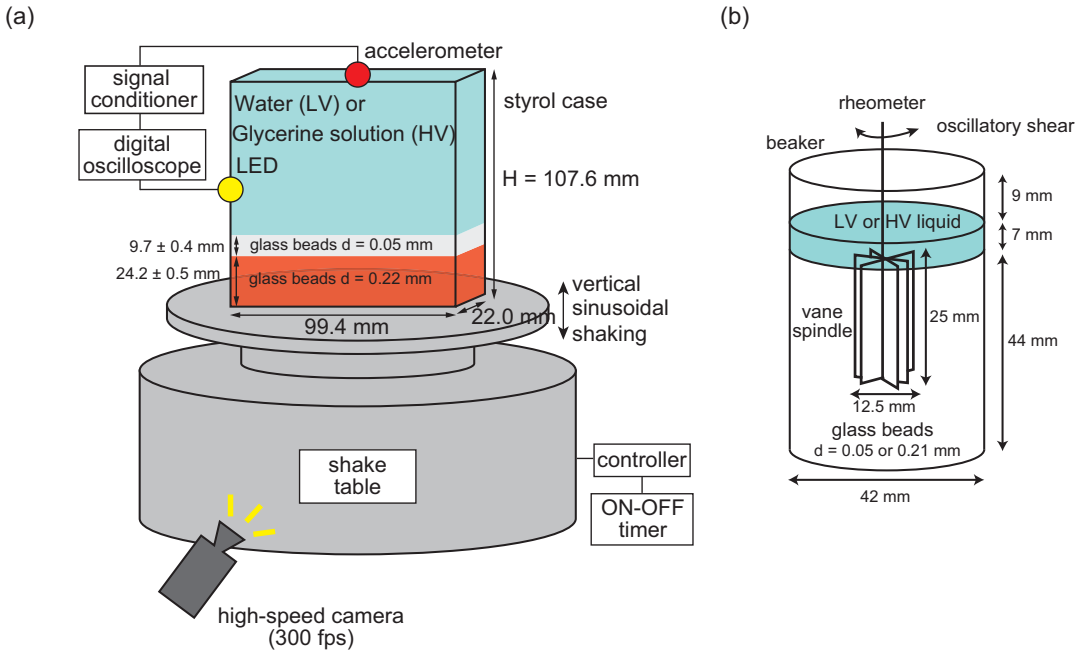

FIG. 1. (a) An experimental setup of the shaking experiments. The thicknesses of the layers are those at the start of shaking and are averages of all experiments (125 runs). LV and HV indicate low- and high-viscosity cases, respectively. d is the particle diameter. (b) Setup for the oscillatory shear rheology measurements.

($d = 0.05 \pm 0.01$ mm) white particles, both having a density of $\rho_p = 2500$ kg/m^3.

Two cells are prepared: a low-viscosity (LV) case which is immersed in water with a viscosity of $\eta = 1$ mPas and a density of $\rho_l = 1000$ kg/m^3, and a high-viscosity (HV) case which is immersed in a glycerine solution with $\eta = 15$ mPas and $\rho_l = 1170$ kg/m^3. The viscosity of the glycerine solution is measured by a rheometer (Physica MCR 301, Anton Paar) in a cone-plate geometry. We confirmed that the viscosity does not depend on the shear rate, i.e., a Newtonian rheology. We add 0.13 vol% of surfactant (Joy, Procter & Gamble) to the liquid to eliminate air bubbles attached to the particles so that particle clustering is avoided. The amount of surfactant added is the minimum required for this purpose. This technique has also been used in previous studies [5].

The initial conditions of the granular medium at the start of shaking for the LV (HV) case are as follows. The lowermost 33.8 ± 0.5 (34.1 ± 0.6) mm of the cell consists of a glass bead layer composed of two size-graded layers. The upper layer with a thickness 9.8 ± 0.3 (9.6 ± 0.6) mm consists of fine white particles and the lower layer with a thickness 24.0 ± 0.4 (24.5 ± 0.5) mm consists of coarse red particles. The thicknesses of the upper and lower layers scaled by d of each layer are $N_{\rm upper} \sim 194$ and $N_{\rm lower} \sim 110$, respectively. The diameters are chosen so that they become size-graded during settling and also to avoid smaller particles fitting into the pore space of the larger particles [3]. The volumetric packing fractions ϕ of the upper and lower layers at the start of shaking are $\phi = 0.60 \pm 0.02$ (0.61 ± 0.04) and $\phi = 0.49 \pm 0.01$ (0.48 ± 0.01), respectively, and are smaller than $\phi \sim 0.64$ for dense random packing of spheres [8], indicating that the particles are initially loosely packed. The error of the layer thicknesses and ϕ described above are calculated from the standard deviation using the measurements of all experiments. We note that the layer thicknesses and the volumetric packing fractions of the two layers for the LV and HV cases are the same within the error.

There are two characteristic velocity scales in our experiments. One is the particle settling velocity in a liquid, which is estimated by the Stokes velocity V_s,

$$V_s = \frac{\Delta\rho g d^2}{18\eta}, \tag{1}$$

where $\Delta\rho = \rho_p - \rho_l$ is the particle-liquid density difference and g is the gravitational acceleration. The other is the volumetric flow rate of the liquid in a porous medium per unit area (i.e., the discharge rate), which is estimated by the Darcy velocity V_D. V_D in a fluidized granular medium is given by [9]

$$V_D = \frac{k}{\eta}\phi\Delta\rho g, \tag{2}$$

where k is the permeability. k is evaluated from the Kozeny-Carman formula (e.g., [10]) as

$$k = \frac{1}{180}\frac{(1-\phi)^3}{\phi^2}d^2, \tag{3}$$

where the prefactor corresponds to the case of spherical particles. Using the d and ϕ values of the upper and lower layers, we estimate that the k of the upper layer is smaller than the k of the lower layer by a factor of $\simeq$60, thus forming a permeability barrier. This estimate shows that the discharge rate can be reduced by more than an order of magnitude when the liquid percolates from the lower to the upper granular layer.

Both V_s [Eq. (1)] and V_D [Eq. (2)] scale as $\propto\Delta\rho/\eta$. As a result the velocity scales of the HV case are smaller than those

of the LV case by a factor of 17. Accordingly, the time scales of the experimental procedure for the HV case are chosen to be a factor of 17 longer than those for the LV case. In what follows, we call this scaling the V_s scaling. Similarly, when we compare the experimental results of the LV and HV cases, the timings of the HV case are chosen to be 17 times longer than those of the LV case. This allows us to clarify how the viscosity dependence deviate from the V_s scaling.

The experimental procedure is as follows. First the cell is thoroughly shaken by hand, and then it is attached to a shake table (Big Wave, Asahi Seisakusyo). The particles are allowed to settle for 300 and 5100 s for the LV and HV cases, respectively, which correspond to $\sim 5.7H/V_s$ and are sufficiently long for all the particles to settle. Then the cell is shaken vertically at a specified acceleration and frequency for 5 and 85 s, for the LV and HV cases, respectively. The vertical displacement z of the shake table changes sinusoidally with time t as

$$z = A \sin 2\pi f t, \tag{4}$$

where A is the amplitude and f is the frequency. An accelerometer (352A24, PCB Piezotronics) is attached to the top of the cell to measure the vertical shaking. The output signal is sent through the signal conditioner (482C05, PCB Piezotronics), and its voltage is recorded by a digital oscilloscope (ZR-RX70, Omron).

We use a high-speed camera (EX-F1, Casio) at 300 fps to record the images. An LED lamp is used to synchronize the acceleration and image data. The recorded data are analyzed using MATLAB. After the shaking starts, the profiles of the granular layer surface and the two-layer boundary change with time. We binarize the images and trace these boundaries, which are then analyzed in detail. The characteristic length scales of the profiles differ according to the shaking condition. We define the length scales after the shaking stops, at $t = 9.9$ s and $t = 168$ s for the LV and HV cases, respectively. These timings are similarly chosen according to the V_s scaling and we hereafter call these the reference times.

We also checked the extent to which the shaking is vertical. We attached accelerometers at the center and the two orthogonal sides of the shake table, and measured the vertical acceleration (a_v) and the two nonvertical accelerations, i.e., front-backward (a_{fb}) and sideways (a_s) components, at all frequencies in the range of 10–5000 Hz used in our shaking experiments. We calculate the ratio of nonvertical to vertical components and find that for most frequencies both a_{fb}/a_v and a_s/a_v are $\leqslant 0.05$. Relatively higher ratios were found as follows: 0.09 ± 0.02 at $f = 100$ Hz, 0.15 ± 0.12 at $f = 150$ Hz, 0.07 ± 0.05 at $f = 2000$ Hz, and 0.08 ± 0.002 at 5000 Hz, where the values are the average and standard deviation of a_{fb}/a_v and a_s/a_v. The existence of nonvertical components implies that the total acceleration $[a_{total} = (a_v^2 + a_{fb}^2 + a_s^2)^{1/2}]$ is slightly larger than a_v by less than 3%.

B. Oscillatory shear rheology measurements

In order to complement the shaking experiments, the fluidization process is also studied using a rheometer to which a six-bladed vane spindle is attached [Fig. 1(b)]. We impose an oscillatory shear to the sample and incrementally increase its stress amplitude (e.g., [11]). Although the sample is sheared horizontally, which differs from our shaking experiments, the rheometer can accurately measure the strain and its phase lag relative to the imposed stress and how they change with the stress amplitude.

The details of the measurements are as follows. A beaker is filled with 80.0 g of glass beads ($d = 0.05$ and 0.21 mm) and 30 cm^3 of water ($\eta = 1$ mPas, LV case) or a glycerine solution ($\eta = 18$ mPas, HV case). Same as the shaking experiments, we add $\sim$0.10 vol% of a surfactant to the liquid to eliminate the bubbles attached to the particles. Adding more surfactant (0.15 vol%) does not affect the rheology. We thoroughly mix the sample and allow the particles to settle for 2.5 and 50 min for the LV and HV cases, respectively. As a result, the lower $\simeq$44 mm becomes a liquid-immersed granular medium and the upper $\simeq$7 mm becomes a clear liquid layer. The packing fraction ϕ of the granular medium is $\phi \simeq 0.58$ for both cases. We insert a vane spindle vertically into the beaker such that the upper end of the spindle coincides with the surface of the granular layer. The spindle rotates around its axis. We impose a shear stress which changes sinusoidally with time $\sigma(t) = \sigma_p \sin 2\pi f_R t$ at $f_R = 100$ Hz and incrementally increase its peak stress amplitude σ_p. We measure the spindle deflection angle $\Delta\omega$ and its phase angle δ, and from $\Delta\omega$, we calculate the bulk strain γ_{bulk} at the surface of the spindle, assuming that the whole sample in the annular region, defined by the spindle and the beaker, deforms.

Storage modulus G' is the elastic component of the modulus (e.g., [12]) and is calculated from

$$G' = \left(\frac{\sigma_p}{\gamma_{bulk}}\right) \cos\delta. \tag{5}$$

The loss modulus G'' is the viscous component and is calculated from

$$G'' = \left(\frac{\sigma_p}{\gamma_{bulk}}\right) \sin\delta. \tag{6}$$

Loss tangent ($\tan\delta$) characterizes the viscoelasticity and is the ratio of these two modulii:

$$\tan\delta = \frac{G''}{G'}. \tag{7}$$

$\tan\delta \ll 1$ indicates a solidlike (elastic) rheology, whereas $\tan\delta \gg 1$ indicates a fluidlike (viscous) rheology.

III. DIMENSIONLESS NUMBERS AND THE PARAMETER SPACE

There are three dimensionless numbers which characterize our experimental conditions. The first is the Stokes number St [1],

$$\mathrm{St} = \frac{t_{micro}^{fall}}{t_{micro}^{visc}} = \frac{V_s}{V_f}. \tag{8}$$

St compares the microscopic time scale for a particle to settle a distance d by free fall t_{micro}^{fall} to the microscopic time scale for a particle to settle d by Stokes settling t_{micro}^{visc} and is expressed by the ratio of the Stokes velocity V_s [Eq. (1)] to the free-fall velocity $V_f = \sqrt{2(\Delta\rho/\rho)gd}$. St $\ll 1$ indicates that viscous drag dominates over particle inertia when the particle settles a

distance $\sim d$. Using the particle diameter of the upper granular layer ($d = 0.05$ mm), we find that St of the LV and HV case experiments are $\mathrm{St} = 8\times10^{-2}$ and $\mathrm{St} = 5\times10^{-3}$, respectively, and thus $\mathrm{St} \ll 1$ for both cases. This is a combined result of small d and large η in our experiments. In contrast for the same d, when the granular medium is air immersed, St is $\mathrm{St} \sim 6 > 1$ and the particle inertia becomes important. The resulting granular dynamics are strikingly different [3].

The second is the dimensionless acceleration Γ, which compares the peak acceleration $\ddot{z}_{\mathrm{peak}}$ to the reduced gravity in the fluid $g' = \Delta\rho g/\rho_{\mathrm{p}}$,

$$\Gamma = \frac{\ddot{z}_{\mathrm{peak}}}{g'} = \frac{A(2\pi f)^2}{\Delta\rho g/\rho_{\mathrm{p}}}. \tag{9}$$

Here we used g' for nondimensionalization to account for the fluid buoyancy. This differs from the commonly used definition for Γ, where g is used (e.g., [13]). Our definition of Γ reduces to the conventional definition of Γ for the air-immersed experiments ($\Delta\rho \simeq \rho_{\mathrm{p}}$).

The third is the viscous number I_{v} (or a dimensionless frequency),

$$I_{\mathrm{v}} = \frac{t^{\mathrm{visc}}_{\mathrm{micro}}}{t_{\mathrm{macro}}} = \frac{f}{V_{\mathrm{s}}/d}, \tag{10}$$

which compares the microscopic time scale for the particles to rearrange by particle settling $t^{\mathrm{visc}}_{\mathrm{micro}} = d/V_{\mathrm{s}}$ to the macroscopic time scale of deformation which is the period of shaking $t_{\mathrm{macro}} = 1/f$ [1,14]. Here we use the Stokes velocity V_{s} to evaluate the microscopic time scale because the experiments are at $\mathrm{St} \ll 1$.

We conducted a total of 73 and 52 experiments for the LV and HV cases respectively, under the following shaking conditions: acceleration of 1.4–78.3 m/s^2 ($0.24 \leqslant \Gamma \leqslant 13.3$) for the LV case and 0.43–40.9 m/s^2 ($0.08 \leqslant \Gamma \leqslant 7.8$) for the HV case. Frequency of $f = 10$–5000 Hz for both cases, corresponding to $0.3 \leqslant I_{\mathrm{v}} \leqslant 123$ for the LV case and $4 \leqslant I_{\mathrm{v}} \leqslant 2083$ for the HV case, where we similarly used the particle diameter of the upper granular layer ($d = 0.05$ mm) to evaluate I_{v}. Thus, our experiments cover $\Gamma \sim O(1)$ and $I_{\mathrm{v}} \sim O(1)$.

There are many other parameters in our experiments. The effects of the cell width and the granular layer thicknesses were briefly studied previously [3]. Effects of cell height H is briefly described in Sec. V B. Effects of horizontal shaking are not studied. We restrict to vertical shaking and focus on the liquid viscosity dependence under different Γ and f.

IV. RESULTS

Results are described in three sections. First we study the liquid viscosity dependence by comparing the LV and HV cases results at the same shaking acceleration (Γ) and frequency (f). Next we proceed to vary Γ and f and study how Γ and f dependencies differ with viscosity. Finally we describe the results of granular rheology measurements under an oscillatory shear and clarify their viscosity dependencies.

A. Liquid viscosity effect under the same shaking condition

1. Instability growth and compaction

Figure 2 and Movie 1 in the Supplemental Material [15] compare the time evolution of the LV case in the left column (a) and the HV case in the right column (b), under the same acceleration of 40.7 ± 0.3 m/s^2 ($\Gamma = 7.4 \pm 0.7$) and a frequency of 40 Hz. Here the timing of each image of the HV case is $\simeq$17 times those of the adjacent image of the LV case following the V_{s} scaling. The shaking starts at $t = 0$ s for both cases and stops at $t = 5$ s for the LV case and $t = 85$ s for the HV case.

First we describe the LV case [Fig. 2(a)]. Here small undulations develop at the two-layer boundary ($t = 1.1$ s), after which about five localized eruptions occur at the surface of the granular medium, a phenomena which we call sand boils. Sand boils are observed above the crests of the instability ($t \sim 1.6$ s; see Movie 1 in the Supplemental Material [15]). The amplitude of the instability at the two-layer boundary increases with time. Figure 2(c) shows a close-up of the image at $t = 5$ s, indicating that the crests of the instability form upward pointed spikes. We call this a flame structure [3], a term that has been used to describe a similar structure preserved in sedimentary rocks and was suggested to have formed in a similar way. Rooted at the tip of the upward pointed spikes, narrow upwellings are observed. We call these plumes because we consider that they result from a buoyancy-driven Rayleigh-Taylor instability (Sec. V C). In Fig. 2(a), we also indicate stages I–III, which are defined using the amplitude of the instability at the two-layer boundary (see the end of this section for details).

We note that the instability has two characteristic horizontal length scales: the wider plume spacing which we call the wavelength λ and the narrow plume widths w. These scales are indicated in Fig. 2(c) and are $\lambda \sim 15$ mm and $w \leqslant 1$ mm. The plumes eventually detach from their stems and remain as red patches in the white upper layer. After the shaking stops at $t = 5$ s, the flame structure remains preserved in the granular medium [$t = 9.9$ s of Fig. 2(a)].

Next we describe the HV case [Fig. 2(b)]. Compared to the LV case, the instability of the HV case is characterized by a shorter wavelength of $\lambda \sim 10$ mm and plumes with a larger head that penetrate further into the upper layer without being detached from their stems [Fig. 2(d)]. On the other hand, we find that the sand boils are suppressed compared to those of the LV case (see Movie 1 in the Supplemental Material [15]). Comparing a pair of images at $t = 2.2$ s for the LV case [Fig. 2(a)] and $t = 37.2$ s for the HV case [Fig. 2(b)], we find that although the real time growth rate is faster for the LV case, when it is V_{s} scaled, the growth rate becomes faster for the HV case.

We binarize these images to trace the surface and the two-layer boundary of the granular medium and obtain their horizontal profiles. Examples of these profiles are indicated by the yellow (light) lines in the reference time ($t = 9.9$ s, 168 s) images of Figs. 2(a) and 2(b), respectively. Superimposed are the profiles at $t = 0$ s, which are indicated by the blue (dark) lines. Comparing the profiles at $t = 0$ s with those at $t = 9.9$ and 168 s, we find that, as a result of shaking, compaction δh of the granular medium occurred, indicated by the white arrows.

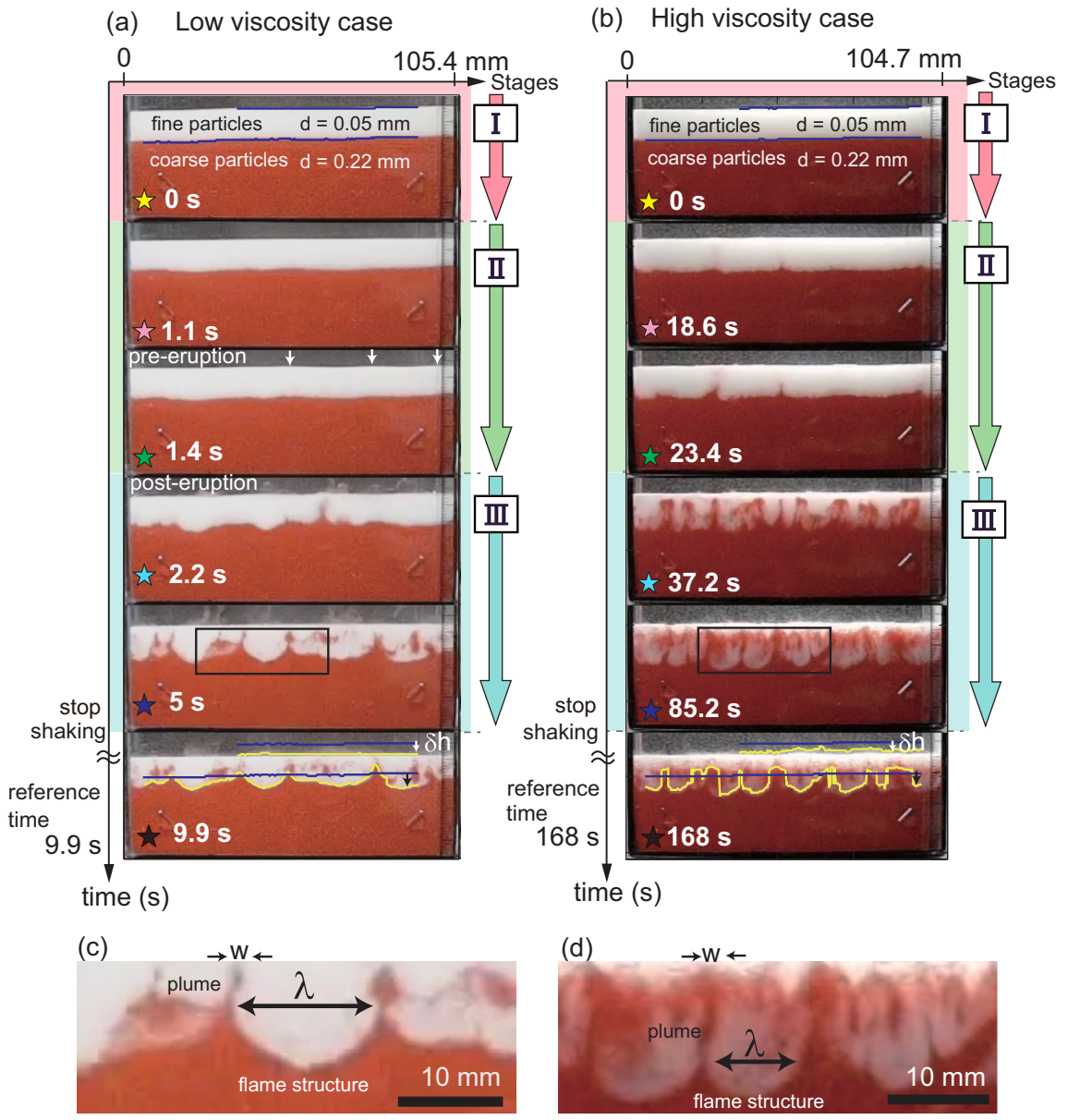

FIG. 2. Comparison of LV (water) and HV (glycerine solution) cases at a shaking condition of 40.7 ± 0.3 m/s^2 ($\Gamma = 7.4 \pm 0.7$) and 40 Hz (see also Movie 1 in the Supplemental Material [15]). The timings of the two cases are scaled by a factor of $\simeq 17$ (V_s scaling). (a) LV case at 40.5 m/s^2 ($\Gamma = 6.9$). (b) HV case at 40.9 m/s^2 ($\Gamma = 7.8$). (c) Close-up of a rectangular section at $t = 5$ s in (a). λ is the instability wavelength, and w is the plume width. (d) Same as (c) but at $t = 85.2$ s in (b). Yellow (light) lines at the reference times $t = 9.9$, 168 s trace the surface of the granular layer and the two-layer boundary. Superimposed blue (dark) horizontal lines are these heights at $t = 0$ s, and vertical arrows indicate the displacements. δh is the compaction of the whole granular layer. I, II, and III indicate the three stages defined using the relative amplitude [Eq. (13)].

Next we calculate the horizontal average of the profile to obtain the average height. We then define the displacement as the height relative to the height at $t = 0$ s. The time evolution of the displacements of the surface and the two-layer boundary are shown in Figs. 3(a) and 3(b) for the LV and HV cases, respectively. The absolute value of the surface displacement corresponds to the compaction (δh) of the whole granular medium.

We point out three features which are evident from Figs. 3(a) and 3(b). First, these figures show that compaction increases with time. As a result of compaction, the packing fraction ϕ of the granular medium increases. From the measured δh at the reference time, which is indicated by a circle in Fig. 3(a), we find that the average ϕ of the whole granular medium increased during this time interval from $\phi = 0.51$ at $t = 0$ s to $\phi = 0.55$ at $t = 9.9$ s. Similarly in Fig. 3(b), ϕ increased from $\phi = 0.51$ at $t = 0$ s to $\phi = 0.55$ at $t = 168$ s. We note that in Fig. 3(a), there is a peak in the surface displacement data indicated by an arrow. This corresponds to the eruption resulting from sand boil. On the other hand, such a peak does not exist in Fig. 3(b), indicating a suppression of sand boil for a HV case. Second, these figures

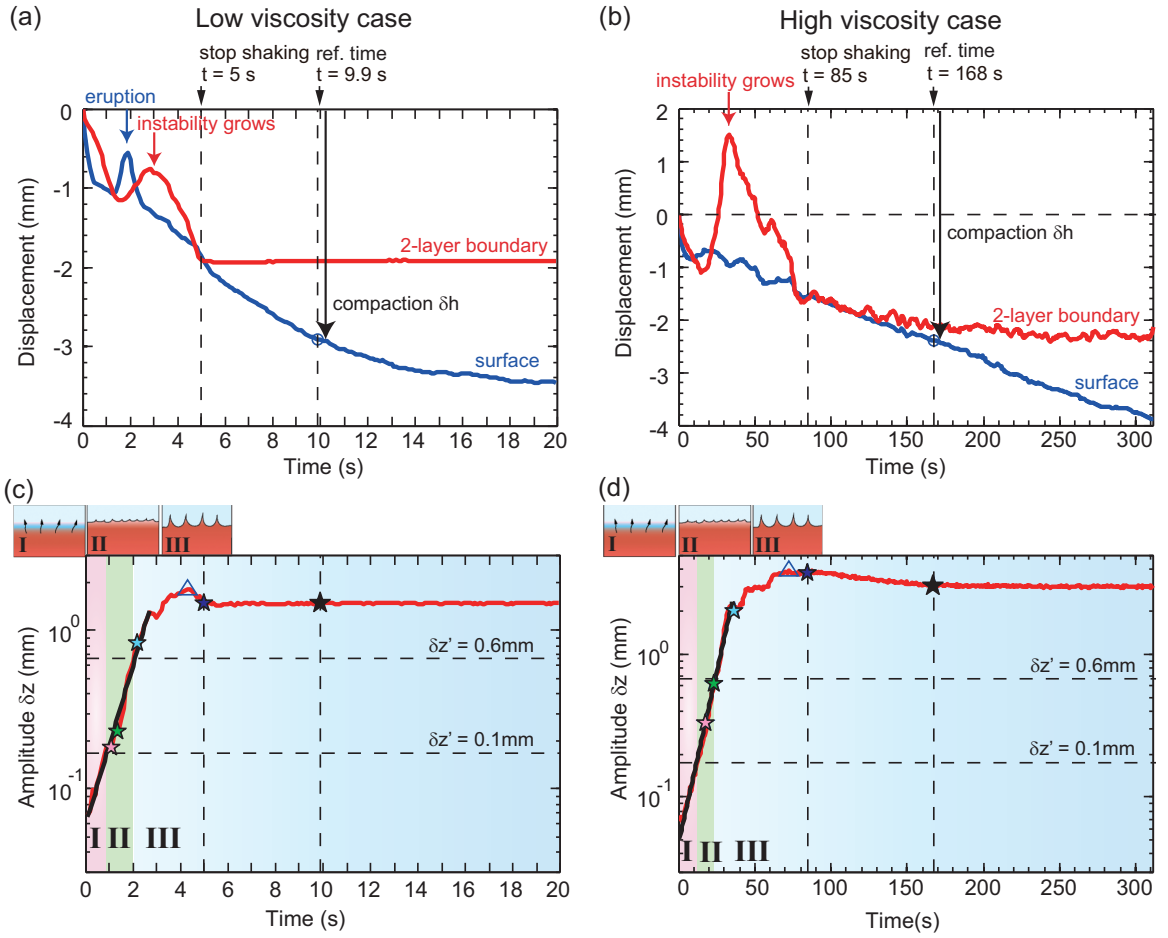

FIG. 3. (a) Displacements (five point running averaged) of the surface (blue) and the two-layer boundary (red) of the granular medium, as a function of time for the LV case shown in Fig. 2(a). A black arrow indicates compaction (δh). (b) Same as (a) but for the HV case shown in Fig. 2(b). (c) Amplitude (δz) of the two-layer boundary for the experiment shown in (a). A triangle indicates the maximum amplitude. Colored stars correspond to the same timing as shown in Fig. 2(a). A black line indicates the exponential fit to the instability growth. I, II, and III indicate the three stages defined using the relative amplitude [Eq. (13)]. (d) Same as (c) but for the experiment shown in (b).

show that when the shaking stops, compaction of the lower layer also stops within a short time, whereas that of the upper layer continues for quite a long time. This indicates that the liquid percolation through the lower layer ends earlier than that of the less permeable upper layer. Third, the two-layer boundary displacements fluctuate up and down and gradually compact. Fluctuation is a combined result of the instability growth, which tends to increase this height, and compaction, which tends to decrease this height. In total the displacement is negative, indicating that the effect of compaction overwhelmed the instability growth. Note also that the peak of the two-layer boundary in Fig. 3(a), indicated by an arrow, is delayed relative to the peak resulting from eruption at the surface.

We next calculate the amplitude of the instability at the two-layer boundary as follows [3]. First we subtract the two-layer boundary profile at $t = 0$ s from each height profile. Next we subtract the linear fit to the profile and define the amplitude δz by its standard deviation. Figures 3(c) and 3(d) show the growth of δz with time. These figures indicate that δz initially increases exponentially with time, but then the amplitude attains a maximum and the growth stops and remains at a constant value after the shaking stops. The instability growth is also evident from an increase of the two-layer boundary heights in Figs. 3(a) and 3(b). The growth ceases from the detachment of the plume heads from their stems.

We fit the initial growth of δz to an exponential function,

$$\delta z = a \exp(pt), \tag{11}$$

to obtain the growth rate p. For the fit we use the time span of longer than 2 and 34 s from the start of shaking for the LV and HV cases, respectively, and choose the time span in which the variance between the data and the fit is minimized. For the data shown in Figs. 3(c) and 3(d), we obtain $p = 1.16$ and 0.11 (1/s) (growth times $1/p = 0.87$ and 9.12 s), respectively, and the fits are indicated by the black lines. In order to clarify the deviation from the V_s scaling, we nondimensionalize p and define a dimensionless growth rate p',

$$p' = \frac{p}{V_s/d}. \tag{12}$$

When we use the particle diameter of the upper layer ($d = 0.05$ mm), p' becomes $p' = 0.028$ and 0.046, respectively, for the LV and HV case data shown here. Note that p' is larger for

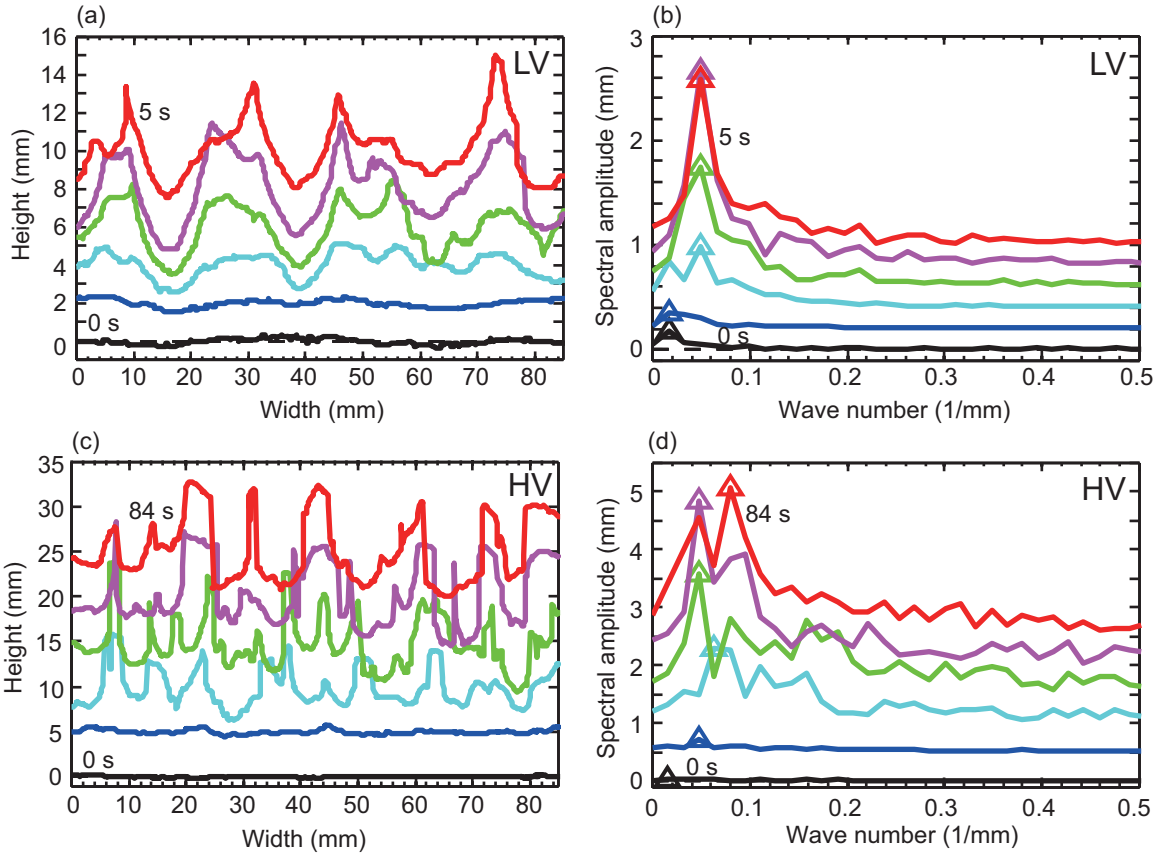

FIG. 4. (a) Evolution of the two-layer boundary profile of the LV case shown in Fig. 2(a) at 1 s intervals between $t = 0$ s and $t = 5$ s. The profiles are incrementally shifted upward by 2 mm. (b) Amplitude spectra of the profiles shown in (a). Triangles indicate the peaks. The spectra are incrementally shifted upward by 0.2 mm. At $t = 5$ s the peak spectral amplitude is 1.6 mm, and its wavelength is $\lambda \simeq 20$ mm. (c),(d) Same as (a),(b) but for the HV case at 16.8-s intervals between $t = 0$ s and $t = 84$ s. The profiles are incrementally shifted upward by 5 and 0.5 mm for (c) and (d), respectively. At $t = 84$ s the peak spectral amplitude is 2.6 mm and its wavelength is $\lambda \simeq 13$ mm.

the HV case, which we recognized from comparing the pairs of V_s scaled images in Fig. 2.

Here we define the relative amplitude $\delta z'$,

$$\delta z' = \delta z - \delta z_0, \tag{13}$$

where δz_0 is the amplitude at $t = 0.1$ s and $t = 1.8$ s for the LV and HV cases, respectively [3]. Using $\delta z'$, we define the following three stages of the instability growth: stage I for $\delta z' < 0.1$ mm, stage II for $0.1 \leqslant \delta z' < 0.6$ mm, and stage III for $\delta z' \geqslant 0.6$ mm. These threshold values were originally defined based on the LV case experiments [3]. We consider that flame structures are fully developed in stage III because for most of the LV case experiments which transition to stage III, a peak amplitude can be identified in the amplitude vs time plot [3]. These stage transitions are indicated in Figs. 2(a) and 2(b) and Figs. 3(c) and 3(d).

2. *Spectral analyses of the two-layer boundary profiles*

We next conduct spectral analyses of the two-layer boundary profiles obtained above. Similar analyses for the instability occurring in a granular medium have been done previously [16,17]. Figures 4(a) and 4(c) show the time evolution of the two-layer boundary profiles of the LV and HV case experiments shown in Figs. 2(a) and 2(b). From these profiles we subtract their linear fits and then calculate their spectral amplitudes using a fast Fourier transform. The results are shown in Figs. 4(b) and 4(d), respectively.

Here we indicate the peak spectral amplitudes by the triangles. For both the LV and the HV cases, at $t = 0$ s the wave number of the peak amplitude is at $\simeq$0.016 1/mm (wavelength $\lambda \simeq 63$ mm), indicating a small wave number (long wavelength) undulation arising from the initial condition. As shaking proceeds, the wave number of the peak spectral amplitude increases with time. The amplitude spectra for the LV case have a well-defined single peak, whereas those of the HV case have multiple peaks. Multiple peaks of the HV case represent the coexistence of the two horizontal scales, i.e., a broad plume spacing and a narrow plume width. Such multiple peaks are absent in the LV case because plumes detach from their stems and the spectral amplitude of the broad plume spacing dominates throughout the experiment. Comparing the LV case spectrum at $t = 5$ s and the HV case spectrum at $t = 84$ s, we find that the peak spectral amplitude and its wave number are larger for the HV case compared to the LV case (see Fig. 4 caption for details), which was evident from comparing Figs. 2(a) and 2(b).

Figure 5 compares the time evolution of the total power (i.e., sum of the power of the whole wave-number range) for the LV and HV cases. Here we scaled the time t using the characteristic

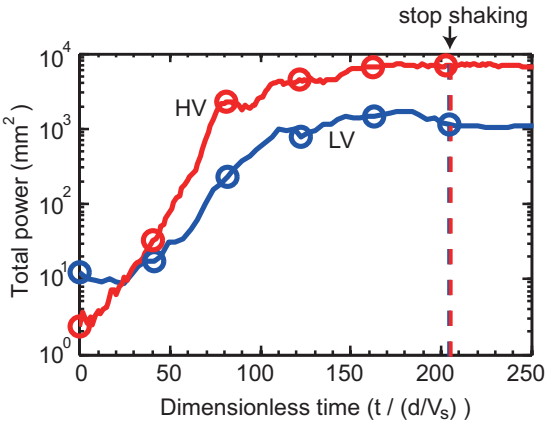

FIG. 5. Time evolution of the total power (power spectrum summed for the whole wave-number range) of the two-layer boundary for the LV and HV cases shown in Fig. 4. Circles correspond to the timing of each amplitude spectrum shown in Fig. 4. Vertical broken lines indicate the timing when the shaking stops.

time d/V_s. The figure confirms a faster V_s scaled growth rate and a larger final total power for the HV case compared to the LV case. The total power is equivalent to the sum of the square of the two-layer boundary profile (Parseval's theorem), which we confirmed for this data set.

3. Comparison from an oblique view

Figure 6 and Movie 2 in the Supplemental Material [15] show the oblique view images of the LV and HV cases at the shaking condition of 41.1 ± 1.4 m/s^2 ($\Gamma = 7.5 \pm 0.9$) and 50 Hz (see Fig. 6 caption for details). Comparing the images we find that several differences are evident. First we note that the eruption from sand boil is suppressed for the HV case, which we noted in Fig. 2 and Movie 1 in the Supplemental Material [15]. Second, there are more red patches at the surface of the granular medium for the HV case compared to the LV case, corresponding to the shorter wavelength of the instability. These red patches appear at the surface of the granular medium soon after the instability appears at the two-layer boundary. Third, for the HV case, a planform of the instability with an upwelling at the center and a downwelling at the rim becomes evident at $t = 27$ s. Such downwellings cannot be discerned for the LV case.

B. Effect of liquid viscosity on acceleration and frequency dependence

1. Amplitude growth and compaction

We now vary the shaking condition and study its effects. First we consider the acceleration dependence. Figures 7(a) and 7(b) show the time evolution of the amplitude δz and the surface displacement (compaction δh indicated by an arrow), respectively, for the HV case. Here the results for different accelerations at a fixed frequency of 40 Hz are shown (see also Movie 3 in the Supplemental Material [15]). Figure 7(a) shows that the initial slope, which corresponds to the growth rate, and the amplitude δz at the reference time ($t = 168$ s) increase with acceleration. Similar to the stages defined in Sec. IVA1, we use the relative amplitude $\delta z'$ [Eq. (13)] at the reference time and classify each experiment into different regimes (see next section for details). Here the 2.0 m/s^2 case is classified as regime II and 5.3–40.9 m/s^2 cases as regime III. Figure 7(b) shows that δh increases with acceleration and that compaction continues even after the shaking stops.

Next we consider the frequency dependence. Figures 8(a) and 8(b) show the time evolution of the amplitude δz and surface displacement for the HV case for different frequencies at a fixed acceleration of 8.01 ± 0.49 m/s^2 ($\Gamma = 1.54 \pm 0.09$).

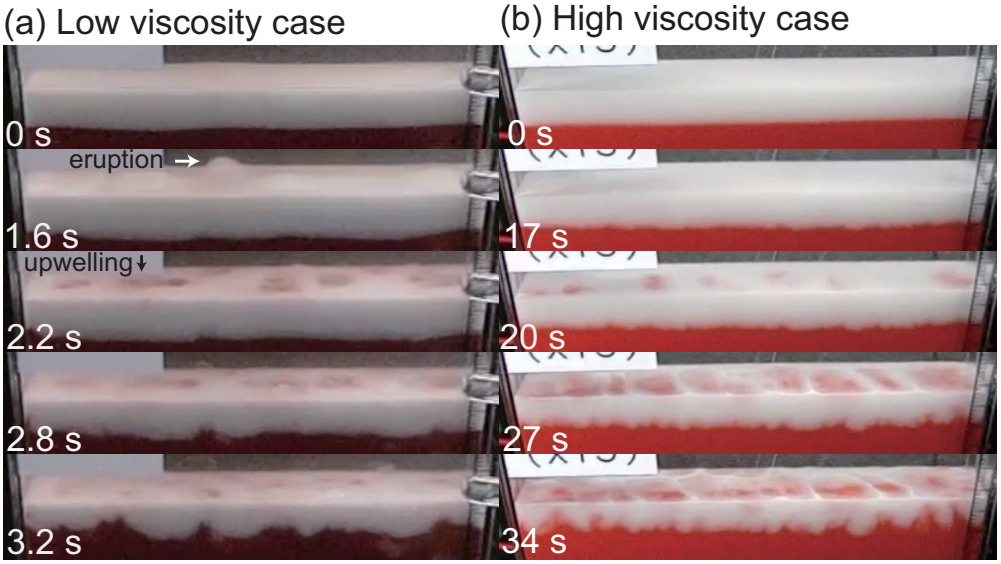

FIG. 6. Oblique view images of the LV and HV cases at 41.4 ± 1.4 m/s^2 ($\Gamma = 7.5 \pm 0.9$) and 50 Hz (see also Movie 2 in the Supplemental Material [15]). The width of the cell is 99.4 mm. (a) LV case at 40.1 m/s^2 ($\Gamma = 6.8$). At $t = 1.6$ s, eruption occurs by sand boil. At $t = 2.2$ s, about seven red patches emerge at the surface which correspond to the upwellings. (b) Same as (a) but for the HV case at 42.1 m/s^2 ($\Gamma = 8.1$). At $t = 27$ s, about 11 upwellings appear. Planforms of the cellular structures are evident, with upwellings (red patches) at the centers and downwellings at the rims.

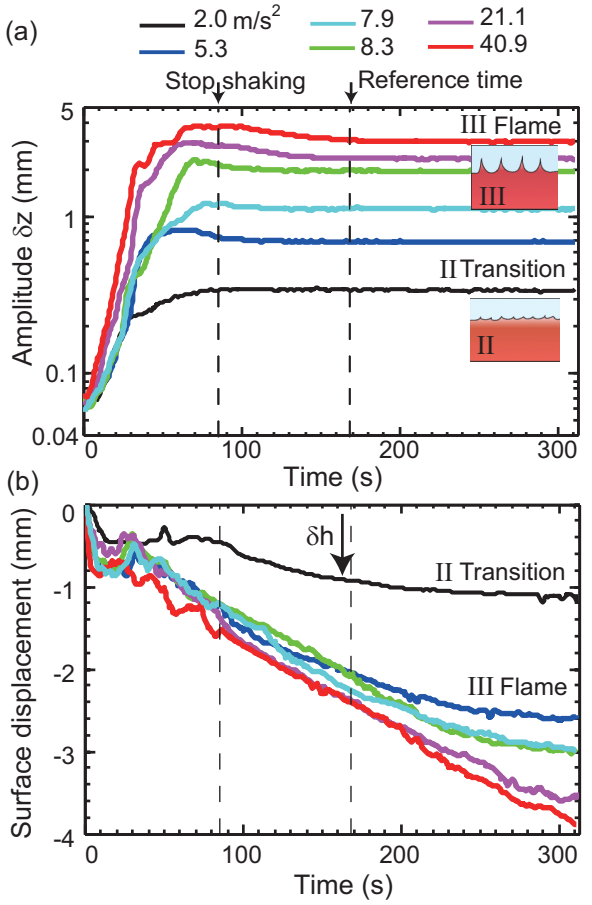

FIG. 7. Acceleration dependence of the (a) amplitude δz at the two-layer boundary and (b) surface displacement (compaction δh indicated by an arrow) of the granular medium for the HV case. Acceleration range is 2.0–40.9 m/s^2 ($0.4 \leqslant \Gamma \leqslant 7.8$) and the frequency is fixed at 40 Hz (see also Movie 3 in the Supplemental Material [15]). Shaking stops at $t = 85$ s. Reference time is $t = 168$ s. Data for 2.0 m/s^2 is in regime IIa (transition with sand boil) and other data are in regime III (flame). Regimes are defined using $\delta z'$ [Eq. (13)] (see Sec. IV B 2 for details).

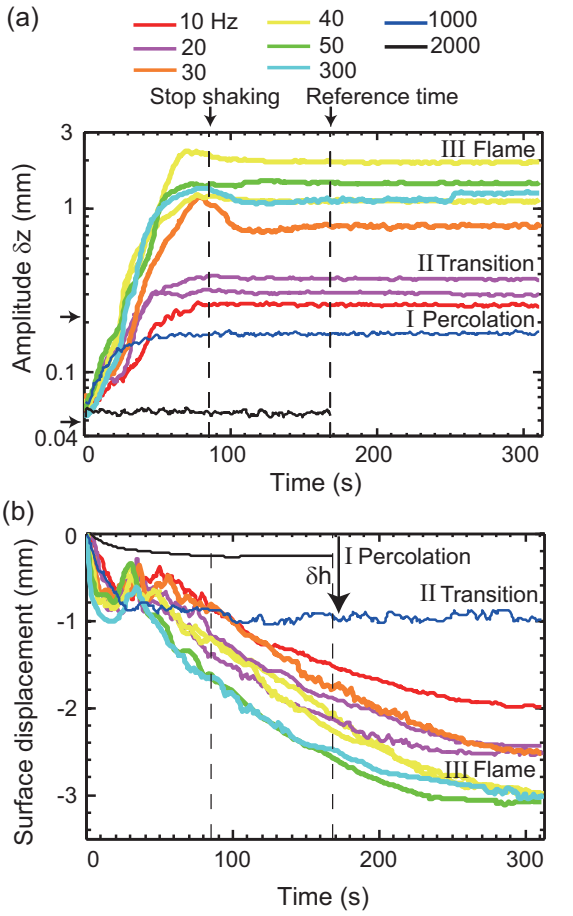

FIG. 8. Frequency dependence of (a) amplitude δz at the two-layer boundary and (b) surface displacement (compaction δh indicated by an arrow) of the granular medium for the HV case. Frequency range is 10–2000 Hz and the acceleration is fixed at 8.01 ± 0.49 m/s^2 ($\Gamma = 1.54 \pm 0.09$). The 1000–2000-Hz data are in regime Ib (percolation), 10–20-Hz data are in regime IIa (transition with sand boil), and 30–300-Hz data are in regime III (flame). Regimes are defined using $\delta z'$ [Eq. (13)] (see Sec. IV B 2 for details).

An important result evident from these figures is that δz and δh at the reference time are largest at the frequency band of 40–300 Hz. This indicates that there is an optimum frequency band for instability growth, or, in other words, the instability growth is frequency selective. Here the 1000–2000-Hz cases are classified as regime I, 10–20-Hz cases as regime II, and 30–300-Hz cases as regime III.

Similar acceleration and frequency dependencies of δz for the LV case were shown previously [3] and are qualitatively the same as the HV case results shown here.

2. *Regime diagrams*

We now summarize all of our shaking experiments in the form of regime diagrams as shown in Fig. 9. The diagrams are plotted in the parameter space of frequency f and dimensionless acceleration Γ [Eq. (9)]. Here the left column shows the LV case and the right column shows the HV case. The experiments are classified into regimes I–III, using the criteria which we describe below, and these are indicated by the different marker shapes. The marker colors (sizes) indicate the magnitude of the relative amplitude $\delta z'$ [Eq. (13)] (top row), dimensionless growth rate p' [Eq. (12)] (middle row), and compaction δh (bottom row). $\delta z'$ and δh are defined at the reference times of $t = 9.9$ s and $t = 168$ s for the LV and HV cases, respectively. p' is calculated from the exponential fit to the amplitude vs time data (Sec. IVA1).

Here we classify the experiments into regimes I–III using the relative amplitude $\delta z'$ [Eq. (13)]. For the threshold values, we use the same values which we used to classify stages I–III (Sec. IVA1) [3]. We further use compaction δh and visual observations to subdivide the regimes. The details are as follows: regime I for $\delta z' < 0.1$ mm, which is subdivided into regime Ia (no change) when $\delta h < 0.1$ mm and regime Ib (percolation) when $\delta h \geqslant 0.1$ mm; regime II for $0.1 \leqslant \delta z' < 0.6$ mm, which is subdivided into regime IIa (transition with sand boil), and IIb (transition without sand boil); and regime III (flame) for $\delta z' \geqslant 0.6$ mm. The threshold of 0.1 mm is close to the pixel size of the images used for the analyses [3]. For all of the experiments in regimes II and III, we find that $\delta h \geqslant 0.1$ mm

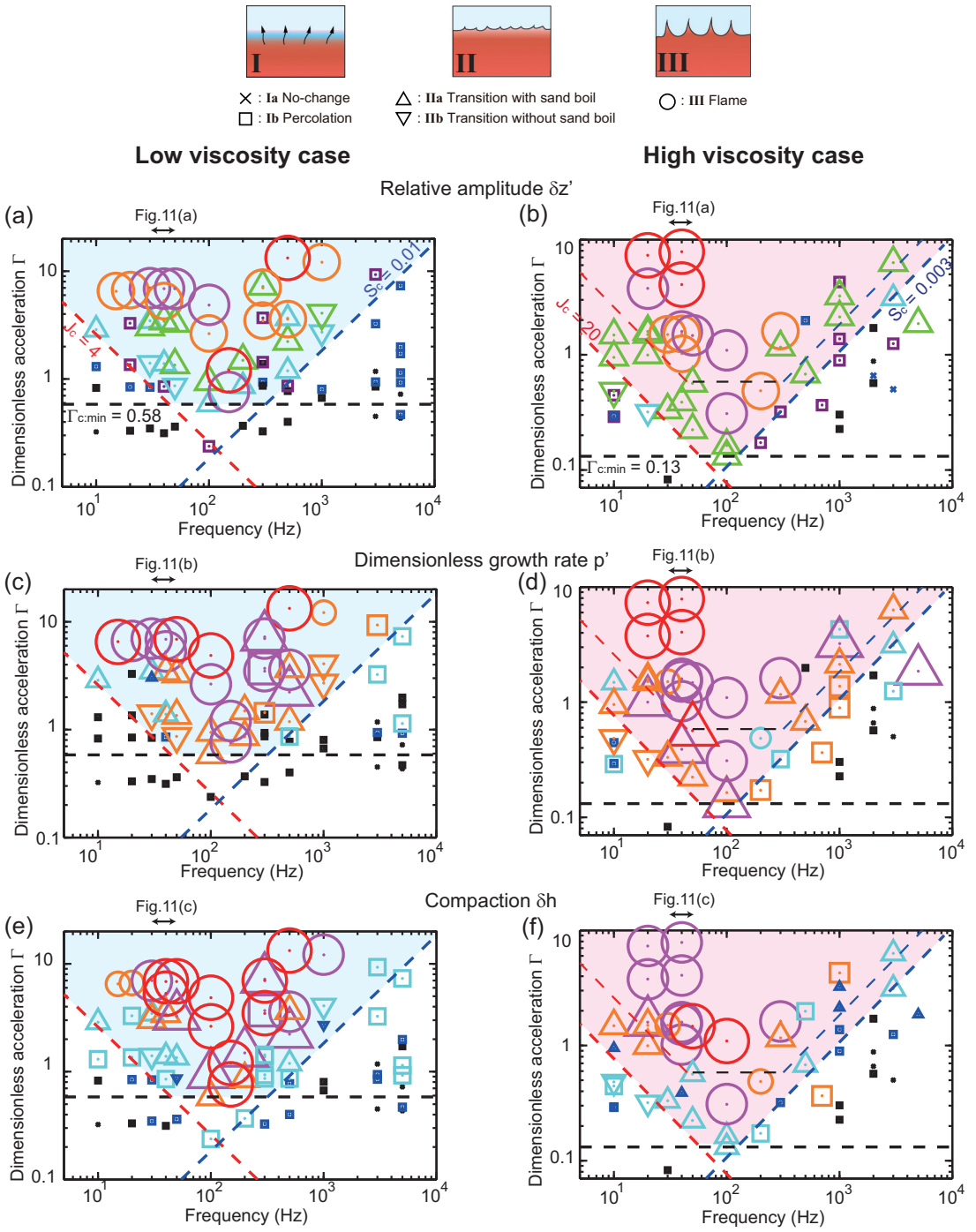

FIG. 9. Regime diagrams of the experiments plotted in the parameter space of shaking frequency and dimensionless acceleration Γ for the LV case (left column, 73 runs) and HV case (right column, 52 runs). Marker shapes indicate the regimes. (a) Relative amplitude ($\delta z'$) of the LV case at the reference time $t = 9.9$ s indicated by the different marker colors (sizes). The ranges of $\delta z'$ (mm) are as follows (in the order of increasing marker size): black, $\delta z' < 0.01$; blue, $0.01 \leqslant \delta z' < 0.05$; purple, $0.05 \leqslant \delta z' < 0.1$; light blue, $0.1 \leqslant \delta z' < 0.15$; green, $0.15 \leqslant \delta z' < 0.6$; orange, $0.6 \leqslant \delta z' < 1.3$; pink, $1.3 \leqslant \delta z' < 2.0$; red, $\delta z' \geqslant 2.0$. The black, blue, and red broken lines indicate $\Gamma_{c:min} = 0.58$, $S_c = 0.01$, and $J_c = 4$, respectively, and the domain defined by $\Gamma > \Gamma_{c:min}$, $S > S_c$, and $J > J_c$, bounded by these three lines, is indicated in blue. (b) Same as (a) but for the HV case at the reference time $t = 168$ s. The black, blue, and red broken lines indicate $\Gamma_{c:min} = 0.13$, $S_c = 0.003$, and $J_c = 20$, respectively, and the domain bounded by these three lines is indicated in pink. The three boundaries in thin broken lines are those of the LV case indicated in (a) and are shown for comparison. (c) Dimensionless growth rate (p') of the LV case indicated by the different marker colors (sizes). The ranges of p' are as follows (in the order of increasing marker size): black, $p' < 0.004$; blue, $0.004 \leqslant p' < 0.006$; light blue, $0.006 \leqslant p' < 0.008$; orange, $0.008 \leqslant p' < 0.02$; pink, $0.02 \leqslant p' < 0.03$; red, $p' \geqslant 0.03$. (d) Same as (c) but for the HV case at $t = 168$ s. (e) Compaction δh (mm) of the LV case at the reference time $t = 9.9$ s indicated by the different marker colors (sizes). The ranges of δh (mm) are as follows (in the order of increasing marker size): black, $\delta h < 0.5$; blue, $0.5 \leqslant \delta h < 1.0$; light blue, $1.0 \leqslant \delta h < 1.5$; orange, $1.5 \leqslant \delta h < 2.0$; pink, $2.0 \leqslant \delta h < 2.5$; and red, $\delta h \geqslant 2.5$. (f) Same as (e) but for the HV case at $t = 168$ s.

and we do not use δh to classify these regimes. We examined the movies of all experiments and visually checked whether sand boil and flame structure formation occurred or not, both of which are indications of instability. We confirmed that for all experiments in regime III, flame structures formed which are preceded by sand boils.

Here we define a developed instability when the relative amplitude is $\delta z' \geqslant 0.1$ mm and sand boils are observed, which corresponds to regimes IIa (upward pointed triangles in Fig. 9) and III (circles in Fig. 9). The three broken lines in Fig. 9 with the slopes of -1 (red), 0 (black), and 1 (blue) are theoretical lines which we derive in Sec. V B, and the domains bounded by these three lines are indicated in blue (LV case) and in pink (HV case). These domains indicate the shaking condition needed for the instability to become developed. On the other hand, outside these domains, regime Ib (squares in Fig. 9) dominates.

We emphasize four important features which are evident from the regime diagrams shown in Fig. 9. First, from Figs. 9(a) and 9(b), we find that the critical Γ (hereafter Γ_c) for the instability to become developed, is minimum at a frequency of $\sim$100 Hz, indicating an optimum frequency band for the instability to develop (see also Movie 4 in the Supplemental Material [15]). Second, from comparing Figs. 9(a) and 9(b), we find that the domain boundary is shifted toward a lower Γ for the HV case compared to the LV case. Third, the above two features are also evident in the plots of the growth rate p' [Figs. 9(c) and 9(d)] and compaction δh [Figs. 9(e) and 9(f)]. Fourth, even when $\Gamma < \Gamma_c$, detectable ($\delta h \geqslant 0.1$ mm) compaction occurs.

The third point suggests that the three characteristic scales $\delta z'$, p', and δh are positively correlated with each other. Accordingly, we plot p' vs $\delta z'$ in Figs. 10(a) and 10(b) and δh vs $\delta z'$ in Figs. 10(c) and 10(d) for the LV and HV cases, respectively. We confirm that good correlations indeed exist among $\delta z'$, p', and δh. The fourth point indicates that liquid percolation is occurring even when the instability is not apparent. We discuss the mechanism of upward liquid transport by permeable flow in Sec. V D.

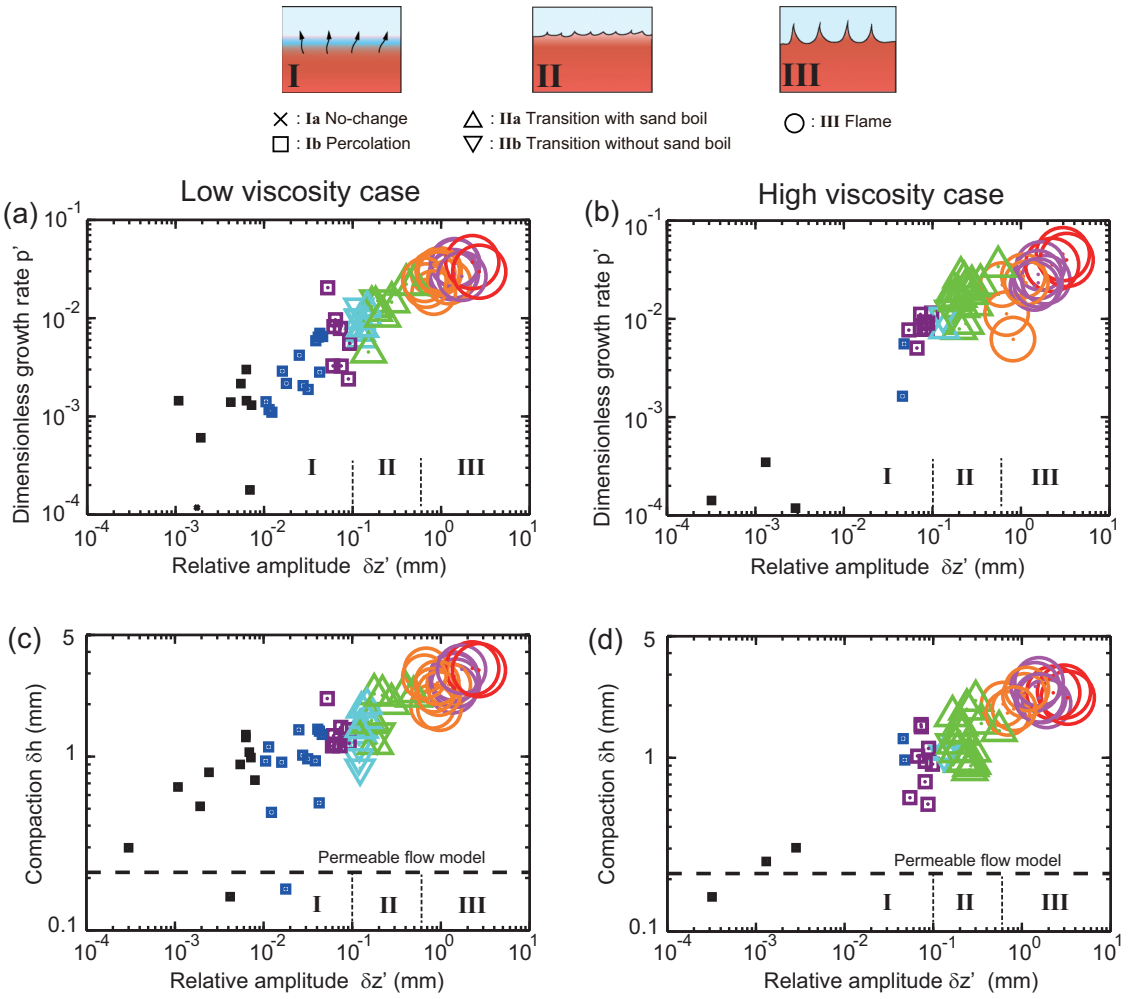

FIG. 10. (a) Dimensionless growth rate p' vs relative amplitude $\delta z'$ (at the reference time $t = 9.9$ s) for the LV case. The marker shapes indicate the regimes, and the colors (sizes) indicate $\delta z'$ and are defined the same as in Fig. 9(a). (b) Same as (a) but for the HV case ($\delta z'$ is at the reference time $t = 168$ s). (c) Compaction δh vs relative amplitude $\delta z'$ for the LV case at the reference time $t = 9.9$ s. A broken horizontal line indicates the compaction calculated using a permeable flow model [Eq. (26)] at $t = 9.9$ s using the parameters for the LV case. (d) Same as (c) but for the HV case at the reference time $t = 168$ s. A broken horizontal line was similarly calculated at $t = 168$ s using the parameters for the HV case.

3. *Comparison of* Γ *dependence for different viscosities*

We next compare the Γ dependence of the LV and HV cases in a narrow frequency band of 40 ± 10 Hz. This frequency band is also indicated by arrows in the regime diagrams (Fig. 9). Figures 11(a)–11(c) show the Γ dependence of the relative amplitude $\delta z'$ [Eq. (13)], dimensionless growth rate p' [Eq. (12)], and compaction δh. As in the previous figures, $\delta z'$ and δh are defined at the reference times, following the V_s scaling. A compilation of several HV case experiments under different accelerations at 40 Hz are also shown in Movie 3 in the Supplemental Material [15]. Figure 11(d) shows the Γ dependence of the wave number of the maximum spectral amplitude. Here the spectral amplitude was calculated from the two-layer boundary profiles using the method described in Sec. IVA2. These figures indicate that at a similar shaking condition, the four characteristic scales of the HV case are larger than or comparable to those of the LV case.

In Figs. 11(a)–11(c) we also indicate the power-law fits. The power-law exponents are larger for the LV case (see caption of Fig. 11), indicating that the differences between the LV and HV cases diminish when Γ becomes large. On the other hand Fig. 11(d) shows that when $\Gamma < 1$, the dominant wave number is small for both cases. This is because the power of the long wavelength depression arising from the initial condition dominates over the short wavelength instability. At $\Gamma > 1$ as the power of the short wavelength instability increases, the wave number of the maximum spectral amplitude also increases. This increase toward a higher wave number occurs at a smaller Γ for the HV case, which is a combined result of a smaller Γ_c [Fig. 11(a)] and a larger wave number [Fig. 4(d)] of the instability for the HV case compared to the LV case.

C. Liquid viscosity effect on granular rheology

Here we describe the results of the oscillatory shear rheology measurements which complement the shaking experiments. The measurements were conducted at a shear frequency of $f_R = 100$ Hz, and the peak shear stress σ_p was incrementally increased as indicated by the rightward pointing arrows in Fig. 12.

Figure 12(a) shows the storage modulus G' [Eq. (5)] as a function of σ_p. Here four samples have similar combinations of particle diameters d and liquid viscosities η as those used in the shaking experiments. The figure shows that G' decreases with σ_p, indicating a shear-thinning rheology. In addition comparing G' under the same σ_p, we find that G' is smaller when d is small and η is large. In particular, we note a precipitous drop of G' for the HV case with $d = 0.05$ mm. Since the particles in these samples are initially jammed, G' depends on the interparticle friction. These results indicate that friction depends systematically on d and η.

In these measurements, the rheometer was programed to impose a stress of up to $\sigma_p = 238$ Pa. However, the actual maximum stresses that can be imposed on these samples indicated by the upward pointing arrows in Fig. 12(a) are in the range of 125–237 Pa and are < 238 Pa. This indicates that these maximum stresses correspond to the yield stress σ_y, above which the granular medium cannot support. Similar to G', σ_y is smaller when d is small and η is large. For comparison

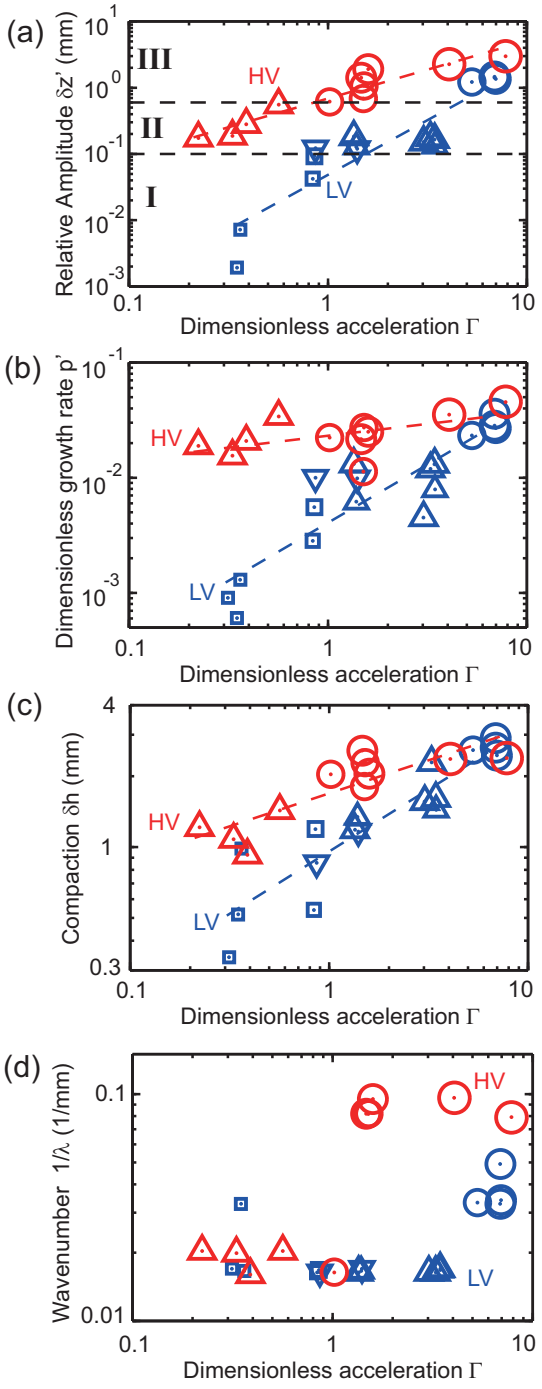

FIG. 11. Comparison of the Γ dependence of instability and compaction for LV (blue) and HV (red) cases at a frequency of 40 ± 10 Hz (see Movie 3 in the Supplemental Material [15] for selected examples from the HV case). Marker shapes correspond to the three regimes indicated in Fig. 9. Broken lines indicate the power-law fits. (a) Relative amplitude $\delta z'$ at the reference times ($t = 9.9$ and 168 s for LV and HV cases, respectively). Broken horizontal lines at $\delta z' = 0.1$, 0.6 mm define the onsets of regime II (triangles) and regime III (circles), respectively. Power-law exponents of the fits are 1.65 (LV) and 0.87 (HV). (b) Dimensionless growth rate p'. Power-law exponents of the fits are 1.01 (LV) and 0.21 (HV). (c) Compaction δh at reference times. Power-law exponents of the fits are 0.53 (LV) and 0.28 (HV). (d) Wave number at which the spectral amplitude attains a peak value.

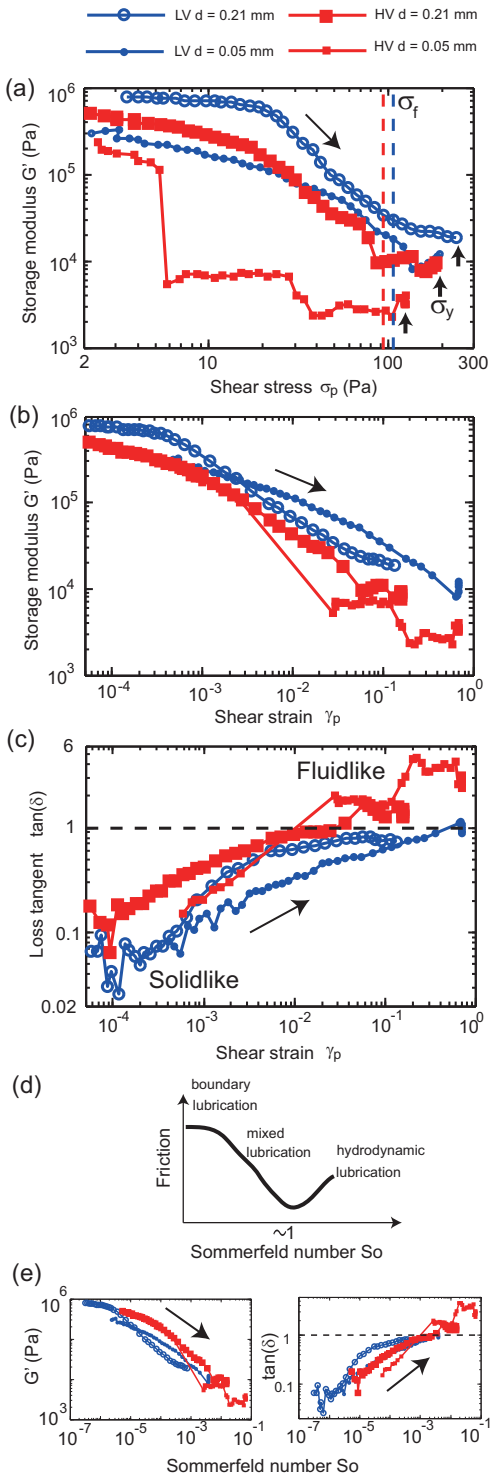

FIG. 12. (a) Storage modulii (G') [Eq. (5)] of the liquid-immersed granular medium as a function of peak stress σ_p measured using the setup shown in Fig. 1(b). Rightward pointing arrows indicate the incremental increase of σ_p during the measurements. σ_y (upward pointing arrow) is the yield stress. σ_f is the frictional stress calculated using Eq. (14) for LV and HV cases. (b) G' plotted as a function of the particle diameter scaled strain γ_p [Eq. (15)]. (c) Loss tangent ($\tan\delta$) [Eq. (7)] plotted as a function of γ_p. A horizontal broken line indicates $\tan\delta = 1$. (d) A schematic Stribeck curve and the three regimes (modified from [19]), as a function of So [Eq. (16)]. (e), (b), and (c) rescaled using So.

in Fig. 12(a), we indicate the estimated frictional stress

$$\sigma_f = \mu\phi\Delta\rho g z \tag{14}$$

by the vertical broken lines. Here $\mu = 0.5$ is the friction coefficient estimated from the angle of repose [18] and z is the inserted depth of the spindle. σ_y and σ_f agree within a factor of 3.

In Fig. 12(b) we replot the data in Fig. 12(a) as a function of particle diameter (d) scaled strain γ_p,

$$\gamma_p = \frac{R\Delta\omega}{d}. \tag{15}$$

Here R is the spindle radius and $\Delta\omega$ is the spindle deflection angle. Since γ_p assumes that the radial extent of deformation is d, it gives an upper bound estimate of strain because the actual shear band thickness is thicker than d, i.e., around $\sim 20d$ [18]. Figure 12(b) shows that G' for different d (0.05 and 0.21 mm) are scaled better in terms of strain γ_p than by stress σ_p. This indicates that, apart from the effect of viscosity, the geometrical configuration of the particles determines G', which was noted previously [11].

In Fig. 12(c), we plot the loss tangent ($\tan\delta$) [Eq. (7)] as a function of γ_p. The figure shows that under a small γ_p, the granular medium is solidlike ($\tan\delta \ll 1$), but as γ_p increases, it becomes more fluidlike ($\tan\delta \sim 1$). The figure shows that at the same γ_p the HV case is more fluidlike. Similar to Fig. 12(b), $\tan\delta$ for different d are scaled better by strain γ_p, rather than by stress σ_p.

Particles used in the measurements of Fig. 12 are all white glass beads. We measured the same rheology for the HV case using red glass beads ($d = 0.22$ mm, $\phi \simeq 0.52$), the same as those used in the shaking experiments. We find that under a shear stress of $\sigma_p \sim 10$ Pa, G' of the red glass beads is the same as that of the white glass beads ($d = 0.21$ mm) within 3%.

V. DISCUSSION

A. Lubrication by a viscous liquid

Fluidization observed in our shaking experiments and rheology measurements can be considered to be a result of lubrication by a viscous liquid between the particles which reduces interparticle friction. Lubrication is well studied in tribology (e.g., [19]). Here we apply these results to our experiments and measurements.

A dimensionless Sommerfeld number (So) is commonly used to evaluate the effect of lubrication [19]. A modified form of So for a granular medium (diameter d) is expressed as

$$\mathrm{So} = \frac{6\eta v}{P_0 d}, \tag{16}$$

where v is the sliding velocity [18] and P_0 is the pressure from the load. It is well known that the friction changes with So, as shown schematically in Fig. 12(d) [19]. This is a result of the thickness of the liquid film between the two sliding solids increasing with So. This curve is known as a Stribeck curve and is characterized by three regimes: a boundary lubrication at $\mathrm{So} \ll 1$ where friction does not depend on So because it is mainly determined by the particle contact; a mixed lubrication at $\mathrm{So} < 1$ where friction decreases with So because of a reduced particle contact; and a hydrodynamic lubrication

at So > 1 where friction increases with So because particle contact becomes small and viscous drag ($\propto \eta v/d$) dominates. As a result the friction becomes smallest at So ~ 1. So has been applied to granular rheology under unidirectional shear, and it was confirmed that friction indeed becomes smallest at So ~ 1 [18].

Similarly, in our shaking experiments and rheology measurements the particles are initially in strong contact (jammed) because they are denser than the liquid. However, when shaken or sheared, the particle contact is loosened and the liquid film thickness between the particles increases (unjammed). Here we evaluate So in our rheology measurements using the peak shearing velocity for v and $P_0 = \sigma_f$ [Eq. (14)]. We rescale the horizontal axis of Figs. 12(b) and 12(c) using So and the results are shown in Fig. 12(e). These figures show that the data for different viscosities collapse fairly well using So. They also show that these measurements were conducted in the range of $10^{-7} <$ So $< 10^{-1}$, suggesting that they are in the mixed lubrication regime. We note that our measurements are conducted under oscillatory shear, and therefore the two figures in Fig. 12(e) are different from the conventional Stribeck curve constructed under unidirectional shear [Fig. 12(d)]. Nevertheless, the reduction of friction in the range of So < 1 suggests a common origin. We note that for dense suspensions ($\phi = 0.5$) but with neutrally buoyant particles, such that the particle contact is small compared to the samples used here, when ϕ is the same, G' is larger for a higher viscosity liquid [11], which is opposite to the result described here [Fig. 12(e)].

Next we estimate So in our shaking experiments. As an upper bound estimate for v, we use the peak velocity of the shake table V which approximates the particle takeoff velocity. The maximum velocity of the shake table is $V \sim 0.3$ m/s. Using $\eta = 15$ mPas, $P_0 \sim 32$ Pa, which is the frictional stress at the depth of the two-layer boundary from the surface of the granular medium, and the particle diameter of the upper granular layer $d = 0.05$ mm, we obtain So ~ 0.2. Since this is an upper bound estimate for So, it indicates that our shaking experiments are also in the mixed lubrication regime (So < 1), possibly including the boundary lubrication regime (So $\ll 1$) at the smallest shaking accelerations. This suggests that in our shaking experiments, particle friction is important but is reduced by lubrication, similar to the rheology measurements shown in Fig. 12.

B. Shaking condition for the instability to grow

We now discuss the origin of the critical acceleration Γ_c for the instability to grow and its frequency dependence. First we summarize our findings. From the shaking experiments, we found that Γ_c is at a minimum at $f \sim 100$ Hz and is smaller for the HV case [Figs. 9(a) and 9(b)]. From the rheology measurements we found that the interparticle friction decreases when the shear strain [Eq. (15)] [or Sommerfeld number So, Eq. (16)] becomes large [Figs. 12(b) and 12(e)] and that the friction decreases with liquid viscosity [Fig. 12(b)].

Combining these results, we infer that the shear strain of the granular medium (equivalently So) becomes largest when it is shaken at an optimum frequency band centered at $f \sim 100$ Hz and that the lubrication by the viscous liquid is a reason for a smaller Γ_c for the HV case. We have previously showed that the frequency dependence for the LV case can be explained by critical values of jerk (time derivative of acceleration) and energy in addition to critical acceleration [3]. In what follows we apply this to both the LV and the HV cases and draw theoretical lines shown in Fig. 9, which approximate the regime boundaries.

First, we consider the minimum critical acceleration $\Gamma_{c:min}$ at $\sim$100 Hz. The black broken lines in Figs. 9(a) and 9(b) indicate $\Gamma_{c:min} = 0.58$ (LV case) and $\Gamma_{c:min} = 0.13$ (HV case), respectively. Our experiments indicate that $\Gamma \geqslant \Gamma_{c:min}$ is a necessary condition for the instability to develop. Since the ratio of inertial stress to the frictional stress is $\sim \Gamma/\mu$ [3], the above necessary condition can be interpreted as the inertial stress needed to overcome friction. A smaller $\Gamma_{c:min}$ for the HV case is consistent with the smaller friction obtained from the rheology measurements [Fig. 12(a)].

Second, we consider the low-frequency limit of the shaking condition needed for the instability to develop. Here we show that this limit is empirically explained by a critical value of jerk, a time derivative of acceleration, which can be nondimensionalized using the characteristic stress and time scales as follows. The frictional stress between the particles scales as $\propto g' = \Delta\rho g/\rho$. On the other hand, the time scale of particle rearrangement scales as $\sim d/V_s$. It follows that the granular medium can balance a jerk of up to $\sim (\Delta\rho g/\rho)/(d/V_s)$ by microscopic readjustment. Using these scales we define a dimensionless jerk J as

$$J = \left(\frac{d^3z}{dt^3}\right)_{\text{peak}} \Big/ \left(\frac{\Delta\rho g}{\rho}\frac{V_s}{d}\right) = \left[\frac{2\pi f}{(\Delta\rho g/\rho)(V_s/d)}\right]^{\dddot{z}}_{\text{peak}} = \left(\frac{2\pi f}{V_s/d}\right)\Gamma = 2\pi I_v \Gamma, \tag{17}$$

where I_v is the dimensionless viscous number (or a dimensionless frequency) [Eq. (10)]. In Figs. 9(a) and 9(b) we show the critical lines for the low-frequency limits (red broken lines) using $J_c = 4$ and $J_c = 20$ for the LV and HV cases, respectively. The scaling used to nondimensionalize jerk is revised from our previous work [3]. J is now expressed using I_v and Γ, and J_c becomes $J_c \sim O(1$–$10)$.

The necessary condition $J = 2\pi I_v \Gamma > J_c$ [Eq. (17)], which approximates the low–frequency limit, implies that for a given Γ there is a lower bound value of I_v. This can be interpreted as follows. We recall that I_v compares the microscopic time scale of particle settling $t_{\text{micro}}^{\text{visc}}$ to the macroscopic time scale of shaking $t_{\text{macro}} = 1/f$ [Eq. (10)]. At very low frequencies ($I_v \ll 1$), particles respond to the change of external forcing by microscopic adjustment, and as a result particles remain close to a jammed state [1]. In our experimental parameter range, the low-frequency limit corresponds to $I_v \sim O(0.1$–$10)$ and is in fair agreement with this interpretation. We also note that at a given f and Γ, J is larger for the HV case, which explains why fluidization is possible at lower frequencies compared to the LV case [compare the two red broken lines for J_c in Fig. 9(b)].

Third, we consider the high-frequency limit of the shaking condition needed for the instability to develop. We define the shaking strength S (e.g., [20]), which corresponds to the shaking energy nondimensionalized by the energy needed to

lift a particle by a height d,

$$S = \frac{A\ddot{z}_{\rm peak}}{\Delta\rho g d/\rho} = \left(\frac{1}{\Delta\rho g d/\rho}\right)\left(\frac{\ddot{z}_{\rm peak}}{2\pi f}\right)^2 = \left(\frac{\Delta\rho g/\rho}{d}\right)\left(\frac{\Gamma}{2\pi f}\right)^2 \propto V^2. \quad (18)$$

Here $V = 2\pi f A$ is the peak shaking velocity. In Figs. 9(a) and 9(b), we show the critical lines for the high-frequency limit (blue broken lines) using $S_c = 0.01$ and 0.003 for the LV and HV cases, respectively. Since $S = 1$ is the shaking energy needed to lift a particle by d, these small ($S_c \ll 1$) values may indicate that particles need only be lifted by $\sim 10^{-3} d$ for fluidization to occur. Here we recall our G' data plotted as a function of strain γ_p [Fig. 12(b)]. The figure showed that friction starts to decrease when the shear displacement is as small as $\sim 10^{-4} d$. This is consistent with the small S_c value obtained above.

The imposed shaking in our experiments has nonvertical acceleration components, i.e., front-backward component a_{fb} and sideways component a_s, in addition to the vertical acceleration component a_v (Sec. II A). Here we discuss their effects. It is possible that the additional shaking originating from the nonvertical components decreased the value of Γ_c compared to the ideal case in which they are zero. However, we show below that it is unlikely that they affected the observed frequency dependence of the low- and high-frequency limits in the range of $f \leqslant 50$ Hz and $f \geqslant 200$ Hz, respectively. At $f \leqslant 50$ Hz, both a_{fb}/a_v and a_s/a_v are small ($\leqslant 0.05$) regardless of frequency. Since the low-frequency limit which scales as $\Gamma_c \propto 1/f$ is observed at $f \leqslant 40$ Hz, we conclude that the imposed nonvertical components did not affect the observed frequency dependence. At $f \geqslant 200$ Hz, a_{fb}/a_v and/or a_s/a_v are relatively large (~ 0.08) at $f = 2000$ and 5000 Hz. However, the high-frequency limit scales as $\Gamma_c \propto f$, which is of the opposite sense to what we expect if the additional nonvertical components at 2000 and 5000 Hz decreases Γ_c. We again conclude that they did not affect the observed frequency dependence. We remark that the same argument also applies to the observed frequency dependence of the growth rate and compaction at $f \leqslant 50$ Hz and $f \geqslant 200$ Hz [Figs. 8 and 9(c)–9(f)]. We also note that if there is a nonzero a_s, it may break the left-right symmetry of the resulting instability. However, in our experiments, sand boils and flame structures are distributed evenly and we do not observe preferential tilting of the plumes toward the left or the right (see Figs. 2 and 6), indicating that such symmetry breaking is apparently absent. We consider that this is a result of the small value of a_s/a_v, and the growth rate [$p < 2$ (1/s)] being smaller than the shaking frequency (10–5000 Hz). The latter implies that because the time scale of the instability growth is long compared to the period of shaking, any symmetry-breaking effect originating from the horizontal shaking is mostly canceled by time averaging.

The nonvertical imposed shaking may be amplified by the resonance of the cell. We attached accelerometers at the front and side walls of the cell and similarly measured a_{fb} and a_s, in addition to a_v. We find that a_{fb} is comparable to or larger than a_s throughout the frequency range of 10–5000 Hz and hereafter consider a_{fb} only. Measurements show that a_{fb}/a_v increases with frequency: $\leqslant 0.3$ at $f \leqslant 50$ Hz, which increases to ~ 0.5–1 at $f = 100$ Hz and ~ 3–6 at $f = 5000$ Hz. Superimposed on this trend, we find a local maximum of $a_{fb}/a_v \sim 6 \pm 2$ at $f = 150$ Hz. It seems that this frequency-dependent a_{fb}/a_v arises from a combined effect of nonvertical components of the imposed shaking and the resonance of the cell. We conducted additional LV case experiments at $\Gamma = 0.84 \pm 0.05$, using a taller cell ($H = 189$ mm) with a similar cross section (99×23 mm) and containing the same amount of glass beads with two diameters. We confirmed the existence of the optimum frequency band for instability growth, but its band was shifted toward a lower frequency centered around $f \sim 40$ Hz. a_{fb}/a_v also increased with frequency with a local maximum ($a_{fb}/a_v = 1.7$) at ~ 40 Hz.

Based on the above measurements, we consider that the combined effect of nonvertical imposed shaking and resonance for the $H = 108$ mm cell used in our experiments differs depending on the frequency range. At low frequencies ($f \leqslant 50$ Hz) this is unimportant ($a_{fb}/a_v < 0.3$). Indeed, transition from regime I to regime II as frequency increases from 10 to 40 Hz occurred without an increase of a_{fb}/a_v. At middle frequencies (100–200 Hz), the nonvertical component becomes comparable to or exceeds the vertical component ($a_{fb}/a_v \sim 0.5$–8). The additional nonvertical acceleration seems to have enhanced the instability growth which lowered $\Gamma_{c:min}$ and shifted the optimum frequency band to include 150 Hz. At high frequencies ($f \geqslant 300$ Hz), although a_{fb}/a_v remains large ($a_{fb}/a_v = 0.6$–6), instability growth is suppressed. We interpret that this is a consequence of the effect of sharply decreasing shaking strength with frequency ($S \propto 1/f^2$) which suppresses fluidization, overwhelming the effect of nonvertical components, which enhances fluidization. To summarize, it is probable that the nonvertical components lowered Γ_c, but otherwise the general features of the frequency dependent Γ_c can be understood by $J \propto f$ [Eq. (17)] and $S \propto 1/f^2$ [Eq. (18)].

C. Application of linear stability analyses for Rayleigh-Taylor instability

The instability observed in our experiments always occurs at the two-layer boundary, and accordingly we consider that it is a Rayleigh-Taylor instability, which occurred due to the accumulation of liquid beneath the less permeable layer. Here we apply the results of the linear stability analyses [21,22] to our experiments. Since the theory was formulated for Newtonian fluids, some modifications and assumptions are needed which we describe below.

Figure 13(a) shows the situation considered. A thin (thickness h), low-density (smaller packing fraction ϕ) lower layer underlies a thick (thickness D), high-density (larger ϕ) upper layer. A thin low-density layer models a fluidized granular layer formed by the accumulation of interstitial liquid beneath the less permeable layer. Such layer has also been called a water film [23]. Since the effective viscosity ($\eta_{\rm eff}$) of the granular medium increases with ϕ [Eq. (20)], the low-density layer is less viscous. A thick high-density layer models the upper layer consisting of finer particles.

The density difference between the two layers $\Delta\rho_{\rm 2layers}$ is expressed as

$$\Delta\rho_{\rm 2layers} = \Delta\phi\Delta\rho, \quad (19)$$

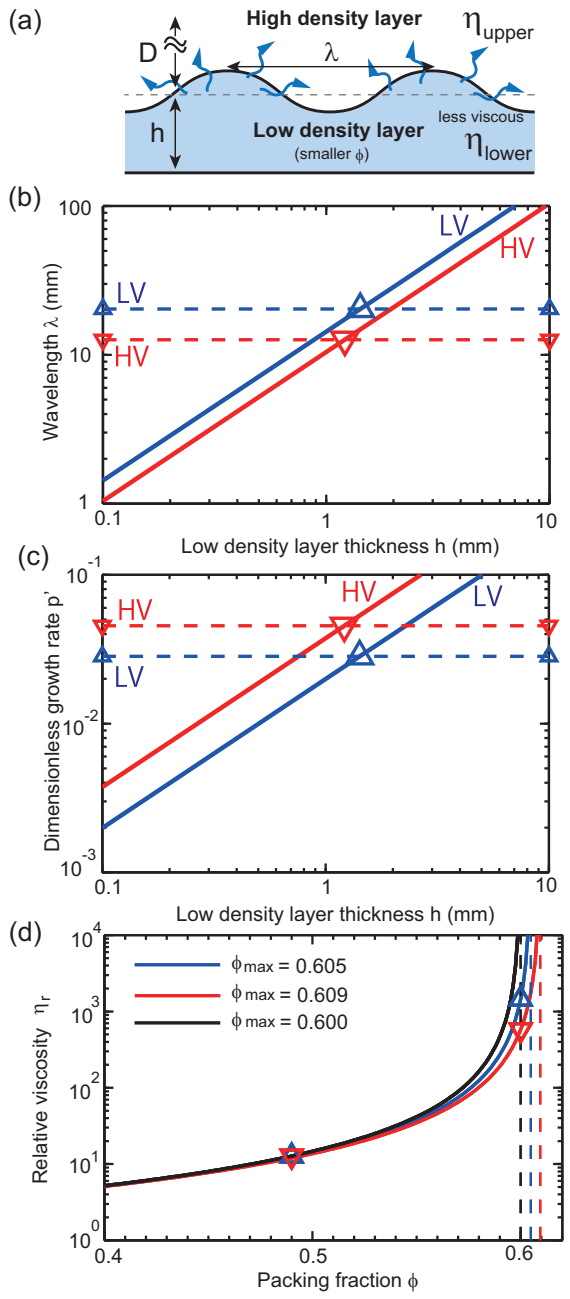

FIG. 13. (a) Schematic diagram (not to scale) showing a situation in which a low-density (small packing fraction ϕ) thin layer (thickness h) underlies a high-density thick layer (thickness D). The lower layer has a smaller viscosity (η) because of a smaller ϕ. A Rayleigh-Taylor instability with a wavelength λ and a permeable flow (arrows) occur at the same time. (b) Wavelength λ and (c) dimensionless growth rate p' as a function of h for LV (blue) and HV (red) cases, calculated using Eqs. (22) and (23). Here the upper to lower layer viscosity ratio $\epsilon = \eta_{\text{eff:upper}}/\eta_{\text{eff:lower}}$ [Eq. (21)] of the LV and HV cases are 117 and 45, respectively. λ and p' values of the experiments shown in Fig. 2 are indicated by the horizontal broken lines. Large triangles at the intersections of the solid and broken lines indicate the solutions for h. (d) Relative viscosity η_r as a function of packing fraction ϕ calculated using Eq. (20) for three values of maximum packing fraction ϕ_{max}. The three broken vertical lines indicate different values of ϕ_{max}. Triangles indicate η_r at $\phi = 0.60$ and 0.49, which are the initial values of ϕ of the upper and lower layers, respectively.

where $\Delta\phi$ is the packing fraction deficit of the low-density layer relative to that of the high-density layer. Fluidized granular medium behaves as a viscous fluid with an effective viscosity η_{eff}. The relative viscosity η_r of the granular medium can be estimated from the Krieger-Dougherty equation (e.g., [12]),

$$\eta_r = \frac{\eta_{\text{eff}}}{\eta} = \left(1 - \frac{\phi}{\phi_{\max}}\right)^{-2.5\phi_{\max}}, \tag{20}$$

where η is the liquid viscosity and $\phi_{\max}$ is the maximum packing fraction. In Fig. 13(d) we show examples of η_r as a function of ϕ for three values of $\phi_{\max}$. We define the effective viscosity ratio ϵ of the two layers as

$$\epsilon = \frac{\eta_{\text{eff:upper}}}{\eta_{\text{eff:lower}}}, \tag{21}$$

where the subscripts indicate upper and lower layers.

Approximate solutions of the wavelength λ and the growth rate p have been obtained under $\epsilon \gg 1$ and a no-slip boundary beneath the thin low-density layer [21,22] as

$$\lambda = 2.92\epsilon^{1/3}h, \tag{22}$$

and

$$p = 0.153\epsilon^{-2/3}\left(\frac{\Delta\rho_{\text{2layer}}gh}{\eta_{\text{eff:lower}}}\right). \tag{23}$$

The dimensionless growth rate p' [Eq. (12)] then scales as $p' = p(d/V_s) \propto p\eta \propto \epsilon^{-2/3}h$. Here we assumed that $\Delta\phi$ and η_r of the lower layer are the same for the LV and HV cases because the initial ϕ for each case is the same, within the error (Sec. II A). Our experiments show that under a similar shaking condition, λ is smaller [Fig. 11(a)], whereas p' is larger [Fig. 11(b)] for the HV case. Here we remark that the scalings $\lambda \propto \epsilon^{1/3}h$ [Eq. (22)] and $p' \propto \epsilon^{-2/3}h$ [Eq. (23)] also indicate an opposite sense of ϵ dependence. Comparing with the experiments, we infer that ϵ is smaller for the HV case.

Here we simultaneously solve Eqs. (22) and (23) by substituting the measured λ and p' to obtain ϵ and h for the LV and HV cases. We note that several assumptions are needed for the calculation, and the obtained ϵ values should be regarded as one possible solution. First, we use Eq. (20) to evaluate $\eta_{\text{eff:lower}}$ in Eq. (23). For the packing fraction ϕ, we use the measured initial values of $\phi = 0.60$ for the upper layer and $\phi = 0.49$ for the lower layer (Sec. II A). $\phi_{\max}$ of the lower layer should be larger than $\phi = 0.49$ because compaction occurs after shaking. We use $\phi_{\max} = 0.600$ for both LV and HV cases, a value between the loose and dense random close packing of spheres [1]. We then solve ϵ and h using λ and p of the experiments shown in Fig. 2 and obtain $\epsilon = 117$, $h = 1.4$ mm for the LV case and $\epsilon = 45$, $h = 1.2$ mm for the HV case. These large ϵ values are consistent with the assumption $\epsilon \gg 1$. Figures 13(b) and 13(c) show λ vs h and p' vs h, calculated using Eqs. (22) and (23), Eq. (12), and above ϵ values. The solutions for h are indicated by large triangles.

An important result is that $h \sim 1$ mm, which corresponds to $\sim 5d$ (lower-layer particle diameter $d = 0.22$ mm). Since the total thickness of the lower granular layer is ~ 24.3 mm, this implies that only a thin layer just beneath the two-layer boundary is mobile. Flow localized in a thickness of $\sim 10d$ or less is a common feature of dense granular flows [1,13,24,25],

and it seems that this is another such example. We also remark that h is comparable to or larger than the measured plume widths of $w \leqslant 1$ mm [see Figs. 2(c) and 2(d)].

Next, using ϵ we solve $\phi_{\max}$ of the upper granular layer from Eq. (20) and obtain $\phi_{\max} = 0.605$ and 0.609 for the LV and HV cases, respectively. Figure 13(d) shows η_r as a function of ϕ using $\phi_{\max} = 0.605$ and 0.609 for the high-density upper layer and $\phi_{\max} = 0.600$ for the low-density lower layer. The figure shows that the difference between these three cases becomes apparent as ϕ approaches $\phi_{\max}$. Among the three cases, $\phi_{\max} = 0.609$, which models the HV case, has the smallest η_r at a given ϕ and models the most shear thinning rheology [26].

When a jammed granular medium is shaken and fluidized, the particle configuration changes toward a more closely packed state and compaction occurs. This corresponds to a change of rheology in which $\phi_{\max}$ increases when a shear is applied. It seems that a smaller interparticle friction for the HV case [Fig. 12(b)] allows more compaction and is at the origin of a larger $\phi_{\max}$. We note that previous measurements of suspension rheology using neutrally buoyant particles have also shown that shear thinning becomes significant when the suspending liquid is more viscous [27].

Finally, using the above estimates of ϵ, we calculate the Reynolds number ($\mathrm{Re} = \bar{\rho} v \lambda / \eta_{\mathrm{eff:upper}}$) of the instability growing in the upper layer. Here $\bar{\rho}$ is the mean density of the granular medium, v is the flow velocity, λ is the wavelength of the instability, and $\eta_{\mathrm{eff:upper}}$ is the effective viscosity. Here we evaluate for the LV case, which gives an upper bound estimate of Re. Using the measured values $v \sim 3\times10^{-4}$ m/s and $\lambda \sim 2\times10^{-2}$ m and the estimated values $\bar{\rho} \sim 1.9\times10^{3}$ kg/m^2 and $\eta_{\mathrm{eff:upper}} \sim 1.5$ Pas, we obtain $\mathrm{Re} \sim 0.01$. A small Re value ($\mathrm{Re} \ll 1$) is consistent with the creeping flow assumption used when deriving Eqs. (22) and (23).

D. Comparison of two liquid ascent mechanisms

In our experiments, there are two mechanisms of liquid ascent which occur simultaneously, the Rayleigh-Taylor instability and permeable flow, as shown schematically in Fig. 13(a). These two mechanisms have different characteristic time scales. Accordingly, we infer that Rayleigh-Taylor instability results only if its time scale is shorter than that of the permeable flow. Here we evaluate these two time scales to constrain the conditions under which either dominates.

First we calculate the dimensionless growth time (τ'_{grow}) of the Rayleigh-Taylor instability. From Eq. (23) we obtain

$$\tau'_{\mathrm{grow}} = \frac{1}{p'} = 6.54\epsilon^{2/3}\left(\frac{\eta_{\mathrm{eff:lower}}}{\Delta\rho_{\mathrm{2layer}} g h}\right)\Big/\left(\frac{d}{V_s}\right) \propto \frac{1}{h}. \quad (24)$$

In Fig. 14 we show τ'_{grow} decreasing with h. Here we used the same ϵ values which we obtained in the previous section for the LV and HV cases.

Next we calculate the dimensionless percolation time (τ'_{perc}) needed for the liquid in the low-density layer to be transported upward by permeable flow until the density difference between the two layers $\Delta\rho_{\mathrm{2layer}}$ [Eq. (19)] becomes zero. From Eqs. (A3) and (A4), we obtain

$$\tau'_{\mathrm{perc}} \sim \left(\frac{\eta}{k\phi_{\mathrm{upper}}\Delta\rho g}\right)\left(\frac{\Delta\phi}{\phi_{\mathrm{lower}}}\right)h\Big/\left(\frac{d}{V_s}\right) \propto h. \quad (25)$$

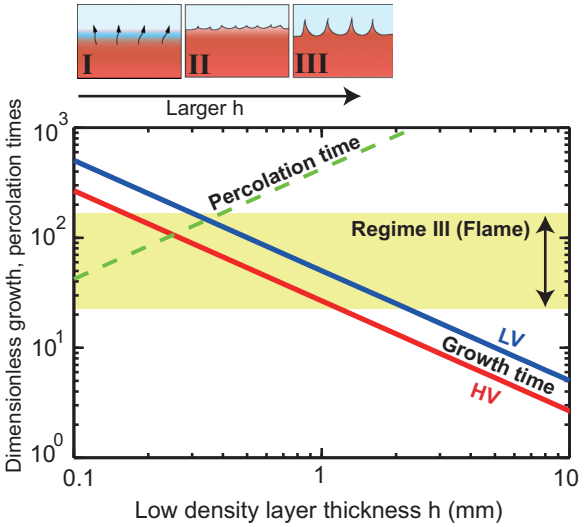

FIG. 14. Dimensionless growth time [Eq. (24)] and percolation time [Eq. (25)] as a function of the low-density layer thickness h. Solid lines indicate growth time for the LV (HV) case using $\epsilon = 117$ ($\epsilon = 45$). These ϵ values are the same as those used in Fig. 13. The broken line indicates percolation time. The measured growth time (dimensionless) in regime III (flame) ($22 \leqslant \tau'_{\mathrm{grow}} \leqslant 161$) is indicated by an arrow. Schematic diagram shows the inferred regime transitions with the increase of h.

In Fig. 14 we show τ'_{perc} increasing with h. Here we used $\Delta\phi = 0.11$ and $\phi_{\mathrm{lower}} = 0.49$ (Sec. V C), the same values used to calculate τ'_{grow} in Fig. 14.

Figure 14 shows that the two time scales, τ'_{grow} and τ'_{perc}, cross over at $h \sim 0.3$ mm, indicating that when $h > 0.3$ mm, Rayleigh-Taylor instability becomes faster than the permeable flow. This thickness is comparable to particle diameter ($d = 0.22$ mm) of the lower layer. In Fig. 14 we also indicate the range of measured dimensionless growth times when the flame structure forms (regime III). We find that the measured time scales overlaps with the estimated time scale, which satisfies $\tau'_{\mathrm{grow}} < \tau'_{\mathrm{perc}}$, indicating that they are consistent. We propose the following scenario as shown schematically in Fig. 14. The thickness h of the fluidized layer beneath the two-layer boundary increases with acceleration (Γ). When h exceeds the critical thickness $h \sim 0.3$ mm, the condition $\tau'_{\mathrm{grow}} < \tau'_{\mathrm{perc}}$ is satisfied, and flame structure develops.

We can further evaluate the contributions from these two mechanisms by comparing the measured compaction with that estimated from permeable flow alone. When the liquid from the low-density layer percolates upward, the upper granular layer will compact. From Eq. (A3) we obtain an expression of compaction δh as a function of time t,

$$\delta h \sim \left(\frac{k\phi_{\mathrm{upper}}\Delta\rho g}{\eta}\right)t. \quad (26)$$

From Eq. (26), we calculate δh at the reference times of $t = 9.9$ and 168 s for the LV and HV cases and obtain $\delta h = 0.22$ mm, which we indicate in Figs. 10(c) and 10(d), respectively. We find that the measured δh is comparable to or larger than the calculated δh. In particular, when flame structures form (regime III cases indicated by circles), δh exceeds this

estimate by about an order of magnitude. This indicates that the discharge rate of a channelized flow resulting from the Rayleigh-Taylor instability is an order of magnitude larger than that by permeable flow alone.

After the shaking stops we may approximate that the liquid transport occurs only by permeable flow through the upper layer. We apply Eq. (A3) to the upper layer to estimate the time scale Δt for the compaction of the upper layer to continue after the shaking stops as

$$\Delta t \sim \left(\frac{\eta}{k\phi_{\mathrm{upper}}\Delta\rho g}\right)\left(\frac{\delta\phi_{\mathrm{upper}}}{\phi_{\mathrm{upper}}}\right)D. \tag{27}$$

Here $\delta\phi_{\mathrm{upper}}$ is the increase of packing fraction of the upper layer by compaction. As an upper bound estimate for $\delta\phi_{\mathrm{upper}}$, we may estimate as $\delta\phi_{\mathrm{upper}} = \phi_{\mathrm{max}} - \phi_0$ where $\phi_{\mathrm{max}} = 0.64$ is the maximum packing fraction for dense random close packing, ϕ_0 is the packing fraction at $t = 0$ s. Substituting the values for the LV and HV cases described in Sec. II A, we obtain upper bound estimates of $\Delta t = 29$ s for the LV case and $\Delta t = 404$ s for the HV case. Experiments indicate $\Delta t \sim 20$ s for the LV case [Fig. 3(a)] and $\Delta t > 300$ s for the HV case [Figs. 3(b), 7(b), and 8(b)]. The above estimate explains why compaction continues for some time after the shaking stops.

E. Comparison with previous experiments

First, we compare our results with those of several previous water-immersed experiments [5,6] that used denser or larger particles compared to those used in our experiments, and, accordingly, the Stokes number St [Eq. (8)] was larger. Leaper *et al.* (2005) [5] studied the shaking condition needed for a mixture of particles with different densities to separate through convection and tilting. They found that as St becomes smaller, the acceleration Γ [Eq. (9)] needed for the separation becomes larger. For the smallest St of $\mathrm{St} \sim 1.0$ in their experiments, Γ becomes $\Gamma \sim 11$. Milburn *et al.* [6] conducted shaking experiments at $\mathrm{St} \sim 17$ and observed that convection and tilting occur when Γ exceeds $\Gamma = 1$–3. Both of these experiments therefore indicate that granular convection and tilting occur at $\mathrm{St} \gtrsim 1$ [1], provided that $\Gamma \gtrsim O(1)$. In contrast, both the LV and the HV cases of our experiments were conducted at $\mathrm{St} \ll 1$ (Sec. III). This suggests that in our experiments, particle inertia was damped by viscosity. Indeed, we confirmed that granular convection and tilting occur in our experimental setup when the particles are air immersed such that $\mathrm{St} \sim 6 > 1$ [3].

Second, we compare the frequency dependence. The experiments mentioned above also showed that the critical Γ for the onset of convection and tilting increases approximately in proportion to frequency, which is similar to our high-frequency limit. Recent experiments using dry granular matter ($\mathrm{St} \sim 600$) have also shown that the onset of convection scales better with shaking velocity V rather than with Γ [28]. Since $V \propto S^{1/2}$, where S is the shaking strength [Eq. (18)], critical V is equivalent to critical S and is also similar to our high-frequency limit. On the other hand, there have been experiments [29] at $\mathrm{St} \sim 420$ which showed a suppression of granular motions at frequencies <12 Hz, which may be similar to our low-frequency limit. However, all of these experiments are at $\mathrm{St} \gtrsim 1$, which differs from the St of our experiments. How the frequency dependence is affected by St deserves further study.

F. Geophysical implications

Based on our experiments, several implications can be drawn with regard to earthquake-induced liquefaction.

First, an optimum frequency band for fluidization to occur implies that apart from acceleration, the frequency spectrum of shaking, which differs among earthquakes, is also important for evaluating the susceptibility to liquefaction. It is well known that there is a minimum earthquake magnitude for earthquake-triggered liquefaction and volcanic eruptions to occur and that this magnitude increases with the distance from the hypocenter [30]. However, the relationship between liquefaction and shaking frequency is still unclear [31]. Both peak ground acceleration, which corresponds to Γ, and peak ground velocity, which scales as $\propto S^{1/2}$ [Eq. (18)], have been conventionally used as indices to estimate the liquefaction risk [31]. Our experiments indicate that both Γ and S need to be considered, and neither one alone is sufficient. In addition, our regime diagram in the parameter space of frequency and Γ (Fig. 9) indicates that instability resulting from liquefaction does not occur at low frequencies, although both Γ and S are large. This indicates that the liquefaction risk is not a simple increasing function of shaking acceleration or velocity.

Second, our experiments indicate that when the interstitial liquid is more viscous, it can lower the critical shaking acceleration for liquefaction to occur by lubrication. This implies that the liquefaction risk becomes higher, provided that the shaking is long enough. This effect may need to be considered when assessing the possibility of liquefaction of particles immersed in viscous liquids such as magma [4].

Third, our experiments showed that a channelized flow resulting from Rayleigh-Taylor instability can result in an order of magnitude increase of compaction of the granular medium [Figs. 10(c) and 10(d)]. This is equivalent to an increase of effective permeability. An order of magnitude increase of permeability has been estimated from field observations [32]. Our experiments provide one plausible mechanism for its origin whenever a less permeable layer exists.

VI. CONCLUSIONS

Vertical shaking experiments using a liquid-immersed, two-layered, size-graded granular medium are conducted in a regime in which the viscous drag is large compared to the particle inertia. Experiments under a wide range of shaking conditions indicate that the critical acceleration needed for fluidization and subsequent instability to grow is at a minimum at a frequency of $\sim$100 Hz. When the liquid viscosity is high, the critical acceleration is smaller, the instability wavelength λ is shorter, and the V_s scaled growth rate is faster. Granular rheology measurements indicate that interparticle friction decreases with shear strain, suggesting that the optimum frequency band for fluidization in our shaking experiments is a consequence of shear strain becoming largest at around 100 Hz. In addition, we find that when the liquid viscosity is high, lubrication reduces friction, which we consider to be a reason

for smaller critical acceleration for the HV case. We showed that this frequency dependence can be explained if we consider that for fluidization to occur, both the jerk (time derivative of acceleration) and the energy of shaking need to exceed their respective critical values. Applying the results of the linear stability analyses for Rayleigh-Taylor instability suggests that only a thin layer beneath the two-layer boundary is mobile, and the viscosity dependence described above originates from the enhanced lubrication and shear thinning when the liquid is more viscous. These are both non-Newtonian features peculiar to a liquid-immersed granular medium.

ACKNOWLEDGMENTS

We thank A. Namiki and Y. Shibano for discussions and the two anonymous referees for their helpful comments. This work was supported by JSPS KAKENHI Grants No. 22109505, No. 24244073, and No. 24510246.

APPENDIX: SIMPLE MODEL OF PERMEABLE FLOW AND COMPACTION

We consider a situation shown in Fig. 13(a) and model the ascent of liquid from a thin low-density layer (thickness h) by permeable flow (arrows). The low-density layer models the fluidized granular layer beneath the two-layer boundary with a packing fraction deficit of $\Delta\phi$ relative to the upper high-density layer. When the low- and high-density layers become fluidized, the overpressure ΔP of the liquid in the low-density layer can be approximated as

$$\Delta P \sim \phi_{\text{upper}} \Delta\rho g (D + h) \sim \phi_{\text{upper}} \Delta\rho g D. \tag{A1}$$

Here we assumed $h \ll D$ since we estimated $h \sim 1$ mm when flame structures form [see Figs. 13(b) and 13(c)] and $D \sim 9.7$ mm. The liquid content of the low-density layer decreases with time as the liquid percolates upward, which can be expressed as

$$\frac{d}{dt} h(1 - \phi_{\text{lower}}) = -V_{\text{D}} = -\frac{k}{\eta}\frac{\Delta P}{D} \sim -\frac{k\phi_{\text{upper}}\Delta\rho g}{\eta}, \tag{A2}$$

where V_{D} is the Darcy velocity [Eq. (2)] and k is the permeability [Eq. (3)] of the upper layer. Since the particle content $h\phi_{\text{lower}}$ is conserved, Eq. (A2) reduces to

$$\frac{dh}{dt} \sim -\frac{k\phi_{\text{upper}}\Delta\rho g}{\eta}. \tag{A3}$$

As the liquid percolates upward, compaction occurs and ϕ_{lower} increases with time. Compaction δh needed for the density difference between the low- and the high-density layers to become zero is

$$\delta h = -dh = \left(\frac{\Delta\phi}{\phi_{\text{lower}}}\right) h. \tag{A4}$$

Substituting Eq. (A4) into Eq. (A3) and rearranging, we obtain Eq. (25), which is an expression for the time needed for the liquid to be transported upward by permeable flow until the density difference vanishes. We also obtain an expression for compaction at an arbitrary elapsed time [Eq. (26)] and by similarly applying to the upper layer to obtain an expression for the time for the compaction to continue after the shaking stops [Eq. (27)].

[1] B. Andreotti, Y. Forterre, and O. Pouliquen, *Granular Media* (Cambridge University Press, Cambridge, UK, 2013).
[2] M. Moretti, P. Alfaro, O. Caselles, and J. A. Canas, Tectonophysics **304**, 369 (1999).
[3] N. Yasuda and I. Sumita, Prog. Earth Planet. Sci. **1**, 13 (2014).
[4] M. Manga and E. Brodsky, Annu. Rev. Earth Planet. Sci. **34**, 263 (2006).
[5] M. C. Leaper, A. J. Smith, M. R. Swift, P. J. King, H. E. Webster, N. J. Miles, and S. W. Kingman, Granular Matter **7**, 57 (2005).
[6] R. J. Milburn, M. A. Naylor, A. J. Smith, M. C. Leaper, K. Good, M. R. Swift, and P. J. King, Phys. Rev. E **71**, 011308 (2005).
[7] C. P. Clement, H. A. Pacheco-Martinez, M. R. Swift, and P. J. King, Europhys. Lett. **91**, 54001 (2010).
[8] G. Mavko, T. Mukerji, and J. Dvorkin, *The Rock Physics Handbook* (Cambridge University Press, Cambridge, UK, 1998).
[9] D. L. Turcotte and G. Schubert, *Geodyamics* (Cambridge University Press, Cambridge, UK, 2014).
[10] J. Bear, *Dynamics of Fluids in Porous Media* (Dover, New York, 1972).
[11] I. Sumita and M. Manga, Earth Planet. Sci. Lett. **269**, 468 (2008).
[12] R. G. Larson, *The Structure and Rheology of Complex Fluids* (Oxford University Press, New York, 1999).
[13] J. Duran, *Sands, Powders, and Grains: An Introduction to the Physics of Granular Materials* (Springer, New York, 2000).
[14] F. Boyer, E. Guazzelli, and O. Pouliquen, Phys. Rev. Lett. **107**, 188301 (2011).
[15] See Supplemental Material at http://link.aps.org/supplemental/10.1103/PhysRevE.93.022901 for the four movies of the experiments and a file explaining their contents.
[16] C. Völtz, W. Pesch, and I. Rehberg, Phys. Rev. E **65**, 011404 (2001).
[17] J. L. Vinningland, Ø. Johnsen, E. G. Flekkøy, R. Toussaint, and K. J. Måløy, Phys. Rev. E **76**, 051306 (2007).
[18] N. Higashi and I. Sumita, J. Geophys. Res. **114**, B04413 (2009).
[19] K. C. Ludema, *Friction, Wear, Lubrication: A Textbook in Tribology* (CRC Press, Boca Raton, FL, 1996).
[20] P. Eshuis, K. van der Weele, D. van der Meer, and D. Lohse, Phys. Rev. Lett. **95**, 258001 (2005).
[21] F. Selig, Geophysics **30**, 633 (1965).
[22] J. A. Whitehead and D. S. Luther, J. Geophys. Res. **80**, 705 (1975).
[23] T. Kokusho, J. Geotech. Geoenviron. Eng. **125**, 817 (1999).
[24] H. Michioka and I. Sumita, Geophys. Res. Lett. **32**, L03309 (2005).
[25] Y. Shibano, A. Namiki, and I. Sumita, Geochem. Geophys. Geosys. **13**, Q03007 (2012).
[26] C. R. Wildemuth and M. C. Williams, Rheol. Acta **23**, 627 (1984).
[27] B. J. Konijn, O. B. J. Sanderink, and N. P. Kruyt, Powder Technol. **266**, 61 (2014).

[28] P. Hejmady, R. Bandyopadhyay, S. Sabhapandit, and A. Dhar, Phys. Rev. E. **86**, 050301 (2012).
[29] G. M. Rodríguez-Liñán and Y. Nahmad-Molinari, Phys. Rev. E. **73**, 011302 (2006).
[30] C.-Y. Wang and M. Manga, Geofluids **10**, 206 (2010).
[31] C.-Y. Wang and M. Manga, *Earthquakes and Water* (Springer-Verlag, Berlin, Heidelberg, 2010).
[32] M. Manga, I. Beresnev, E. E. Brodsky, D. Elkhoury, J. E. Elsworth, S. E. Ingebritsen, D. C. Mays, and C.-Y. Wang, Rev. Geophys. **50**, RG2004 (2012).